SUPPORTING INFORMATION

Optically reversible room-temperature solid-state cobalt(III) photoswitch based on nitro-to-nitrito linkage isomerism

Krystyna A. Deresz,[a] Radosław Kamiński,[a] Sylwia E. Kutniewska,[a]
Adam Krówczyński,[a] Dominik Schaniel,[b] Katarzyna N. Jarzembska [a]*

[a] Department of Chemistry, University of Warsaw, Żwirki i Wigury 101, 02-089 Warsaw, Poland

[b] Université de Lorraine, CNRS, CRM^2, 54000 Nancy, France

* Corresponding author: Katarzyna N. Jarzembska (katarzyna.jarzembska@uw.edu.pl)

1S. Synthesis

The studied [Co(Me-dpt)(NO_2)$_3$] (Me-dpt = 3,3'-diamino-*N*-methylpropanediamine) complex was prepared according to the literature procedure.[1] A mixture of 4.35 g (18.3 mmol) $CoCl_2$ hexahydrate in 15 mL of distilled H_2O was added to the mixture of 2.75 g (18.9 mmol) 3,3'-diamino-*N*-methylopropandiamine in 5 mL of distilled H_2O and stirred overnight while aerating. Then the 4.65 g (54.6 mmol) of KNO_2 dissolved in 3.5 mL of distilled H_2O was added and the mixture was heated to 100°C for next 30 min. The solution was then cooled to the room temperature and active carbon was added and the mixture was heated to boil. Next the solution was filtrated and left for crystallization. The orange, regular single crystals were obtained.

Nuclear magnetic resonance (NMR) spectrum was measured with an Agilent NMR 400 MHz Varian spectrometer; ^{1}H chemical shifts are given relative to TMS by using residual solvent resonances. The ^{1}H NMR spectra in $CDCl_3$ show broadened signals, which may attributed to a reversible NO_2 group dynamics in solution. Elemental analyses were carried out with an Elementar Vario EL III analyser. ^{1}H NMR ($CDCl_3$, 400 MHz): δ = 5.65−5.05 (br, 4H, NH_2), 3.33−3.11 (m, 4H, N-CH_2), 3.03−2.55 (m, 4H, NH_2-$\underline{CH_2}$), 2.20−2.18 (bs, 3H, N-CH_3), 1.83−1.97 (m, 4H, CH_2) ppm. Elemental analysis: $C_7H_{19}N_6Co_1O_6$ (342.21); calculated: C 24.57%, H 5.60%, N 24.56%; found: C 24.33%, H 5.69%, N 24.20%.

2S. X-ray diffraction

All X-ray diffraction experiments (including the preliminary ones) were carried out on a Rigaku Oxford Diffraction SuperNova single-crystal diffractometer equipped with the CCD detector, copper microfocus X-ray source, low-temperature nitrogen gas-flow Oxford Cryosystems device and our homemade light-delivery device[2] allowing *in situ* photocrystallographic experiments. The optimal data collection strategy took into account the mounted light-delivery device and was prepared using the native diffractometer software. For photocrystallographic experiments the same strategy was used. All data collections were carried out in complete darkness (the sample mounting and centring was done prior to any further data collections; all other manipulations were performed with all diffractometer lights permanently switched off). The procedure used during photocrystallographic was as follows: (i) crystal mounting at room temperature (in this contribution all experimenters were performed at room temperature), (ii) data collection with all lights off, (iii) light irradiation for about 2 hours using the previously selected LED with central wavelength of either 470 or 660 nm, respectively (Thorlabs fiber-coupled LEDs: M470F3 or M660F1, correspondingly; light delivered through the 400-μm-core multimode solarisation-resistant fibre optics); during light irradiation the crystal was continuously rotated to ensure the most uniform exposure. No colour changes were observed for crystals upon exposure to LED light. For exact photocrystallographic data collection codes and the measurements sequence for each sample see Table 2S. Data processing (*i.e.* unit-cell determination, raw diffraction-frame integration, absorption correction, scaling) was the same for all data collections. All structures were solved using an intrinsic phasing method as implemented in the *SHELXT* program[3] and refined with the *JANA* package[4] within the independent atom model (IAM) approximation. The disordered structures were modelled using a standard splitting model, in which the initial positions of the metastable linkage isomer atoms were determined from the residual or photodifference maps.[5, 6] These maps are computed as Fourier difference maps following the formula:

$$\Delta\varrho_{\mathrm{phd}} = \frac{1}{V}\sum_{\mathbf{h}}\left(\left|F_{\mathrm{o}}^{\mathrm{ON}}(\mathbf{h})\right|e^{\mathrm{i}\varphi_{\mathrm{c}}^{\mathrm{ON}}(\mathbf{h})} - \left|F_{\mathrm{o}}^{\mathrm{OFF}}(\mathbf{h})\right|e^{\mathrm{i}\varphi_{\mathrm{c}}^{\mathrm{OFF}}(\mathbf{h})}\right)e^{-2\pi\mathrm{i}\mathbf{hr}},$$

where V is the unit cell volume (for computing the map we assume it is approximately the same for both irradiated, ON, and non-irradiated, OFF, crystal structures), **h**'s are the measured reflections, F's are the structure factors (subscript "o" stands for observed, "c" for calculated), φ's are phases. For computing the map we frequently assume only one set of phases, thus $e^{i\varphi_c^{OFF}(\mathbf{h})} = e^{i\varphi_c^{ON}(\mathbf{h})}$. In this contribution we use two sets of ON structures, after 470 and 660 nm LED-light irradiation; maps are computed in the same way. Photodifference maps show structural changes occurring during the light exposure.

All the final refinement statistics are summarized in Table 2S. The CIF files are present in the Supporting Information, or can be retrieved from the Cambridge Structural Database (CSD) (deposition numbers: CCDC 2171480−2171486).[7, 8]

Powder X-ray diffraction (PXRD) measurement was carried out on a Bruker AXS D8 Discover powder diffractometer equipped with a VÅNTEC-1 detector and the copper X-ray tube. Data set was collected in a parallel-beam geometry (locked-couple experiment mode) in the 2θ range from 3 to 40° with scan speed set to 1° per minute. Le Bail refinement[9] of the unit-cell and powder-profile parameters was accomplished with the *JANA* program.[10]

3S. Spectroscopy

All infrared (IR) measurements were performed using a Nicolet 5700 FT-IR spectrometer (spectral resolution of 2 cm^{-1} in the range of 360–4000 cm^{-1}). The sample was fine-grinded, mixed with a spectroscopic-grade KBr, pressed into pellets, and placed in the home-made holder for solid-state samples. Irradiation of the sample was achieved using various LEDs (Thorlabs L and LP series), central wavelengths of which covered the range from violet to red (from 385 to 735 nm). Alternatively to diodes continuous-wave lasers were used for this task.

Reaction conversion was estimated based on the analysis of the 781 cm^{-1} band, attributed to the $\delta(NO_2)$ scissoring vibration of the nitro ligand (see the computational part). It is the best isolated band in the collected IR spectra with the highest contribution of vibrations of the photoswitchable nitro group. Area of the corresponding peak for the 'dark' sample was assigned to the 88% population of the nitro binding mode as indicated by the X-ray diffraction data (12% of the *endo*-nitrito form and 88% of the nitro isomer). This band

decreases along with the nitro-to-nitrito photoisomerisation reaction progress. The nitro isomer population was assumed to be proportional to the intensity of this band. As a consequence, the reaction conversion was estimated based on the relative area of the 781 cm^{-1} band (area of the band in the IR spectrum of the initial sample vs. the corresponding value calculated from the IR spectrum of the irradiated sample).

UV-Vis absorption spectroscopy measurements were performed with a CARY 4000 spectrometer in the 200–900 nm wavelength range. The sample was prepared in the same way as for the IR measurements, and irradiation was conducted using the same set of LEDs or laser sources. Light penetration depth was also obtained from these measurements. Absorbance of the cobalt complex in the KBr 'solution' was used to compute the single-crystal linear absorption coefficient, which gave the penetration depth of about 60 μm (we defined light penetration depth as $I/I_0 = 10^{-3}$, I – intensity of light passing though the sample, I_0 – incident light intensity). Note the penetration depth may be in fact larger since the KBr matrix diffuse scattering contribution to the UV-Vis spectrum was not taken into account.

4S. Computations

All computations were carried out using the *GAUSSIAN* package (*GAUSSIAN16* version).[11] In the case of quantum-mechanics / molecular-mechanics (QM/MM) method, the crystal environment was modelled by cutting out a shell with a radius of 12 Å around the central molecule from the examined experimental crystal structure,[12] in which the C–H distances were set to the neutron-normalized values.[13, 14] The density functional level of theory was applied for the optimization of the central molecule DFT(B3LYP)/6-311++G**,[15-20] whereas the molecular shell was kept fixed and approximated with the Universal Force Field (UFF)[21] employing Hirshfeld atomic charges[22] derived initially at the same level of theory, including both the functional and the basis set. Dimer interaction energies, isolated-molecule geometry optimizations and normal-mode frequencies were also calculated at the DFT(B3LYP)/6-311++G** level of theory. For harmonic mode computations no imaginary frequencies were found for optimized geometries. In the case of interaction energy calculations the Grimme empirical dispersion correction,[23, 24] modified by the Becke-Johnson damping function[25, 26] and correction for BSSE[27, 28] were applied. The automatic generation of input files was accomplished with the *CLUSTERGEN* program.[29]

Table 1S. LED and laser powers (P) used in all experiments presented in the paper.

Experiment type	*Light source*	*Intensity / mA*	*Wavelength*, λ / nm	*Power*, P / mW
X-ray diffraction	LED	1000	470	3.1
	LED	1200	660	2.2
IR and UV-Vis spectroscopy	LED	1000	470	80
	LED	1200	660	86
	laser		476	90
	laser		655	135

Table 2S. Selected X-ray data collection, processing and refinement parameters for all presented crystal structures.

Data set	**100K-dark** [a]	**RT-dark** [b]	**RT-irr470nm-1stRUN** [c]	**RT-irr660nm-1stRUN** [d]	**RT-irr470nm-2ndRUN** [e]	**RT-irr660nm-2ndRUN** [f]
Moiety formula	$C_7H_{19}CoN_6O_6$	– [g]	– [g]	– [g]	– [g]	– [g]
Moiety formula mass, M_r / a.u.	342.21	– [g]	– [g]	– [g]	– [g]	– [g]
Crystal system	orthorhombic	– [g]	– [g]	– [g]	– [g]	– [g]
Space group	$Pca2_1$ (no. 29)	– [g]	– [g]	– [g]	– [g]	– [g]
Z	4	– [g]	– [g]	– [g]	– [g]	– [g]
F_{000}	712	– [g]	– [g]	– [g]	– [g]	– [g]
Crystal colour & shape	Orange block	Orange plate	– [g]	– [g]	– [g]	– [g]
Crystal size / mm^3	0.18×0.15×0.06	0.18×0.16×0.06	– [g]	– [g]	– [g]	– [g]
T / K	100	298	– [g]	– [g]	– [g]	– [g]
a / Å	12.7442(6)	12.8116(11)	12.9023(8)	12.8539(7)	12.8959(8)	12.8611(7)
b / Å	10.7342(5)	10.7825(9)	10.7957(6)	10.7924(5)	10.7975(6)	10.7902(6)
c / Å	9.7366(4)	9.8623(10)	9.8304(6)	9.8369(6)	9.8301(6)	9.8361(6)
V / Å^3	1331.96(10)	1362.4(2)	1369.27(14)	1364.62(13)	1368.78(14)	1364.99(13)
d_{calc} / g·cm^{-3}	1.647	1.644	1.640	1.637	1.634	1.630
θ range	4.08° – 75.81°	4.07° –73.94°	4.06° – 73.87°	4.07° – 74.74°	4.06° – 75.86°	4.07° – 74.07°
Absorption coefficient, μ / mm^{-1}	10.482	10.248	10.196	10.231	10.200	10.228
No. of reflections collected / unique	8689 / 2771	5823 / 2835	5974 / 2879	5933 / 2856	5944 / 2879	5969 / 2856
R_{int}	5.21%	3.55%	4.59%	6.24%	6.87%	4.42%
No. of reflections with $I > 3\sigma(I)$	2273	1506	1951	1991	1826	1927
No. of parameters / restraints / constraints	189 / 0 / 87	189 / 0 / 87	177 / 1 / 99	189 / 0 / 87	177 / 1 / 99	189 / 0 / 87
$R[F]$ ($I > 3\sigma(I)$)	6.90%	7.42%	8.97%	9.23%	9.90%	8.42%
$R[F]$ (all data)	7.76%	8.42%	10.46%	10.37%	11.73%	9.78%
$\varrho_{res}^{min/max}$ / e·Å^{-3}	−0.58 / +1.01	−0.49 / +0.63	−0.51 / +1.05	−0.47 / +0.77	−0.52 / +1.07	−0.41 / +0.92
CCDC code	2171480	2171481	2171482	2171484	2171483	2171486

[a] Experiment at 100 K, not mentioned in the main text (CIF file is attached and deposited to CSD). [b] Experiment No. 0 in Table 2 in the main text. [c] Experiment No. 1 in Table 2 in the main text. [d] Experiment No. 2 in Table 2 in the main text. [e] Experiment No. 3 in Table 2 in the main text. [f] Experiment No. 4 in Table 2 in the main text. [g] Redundant data are omitted.

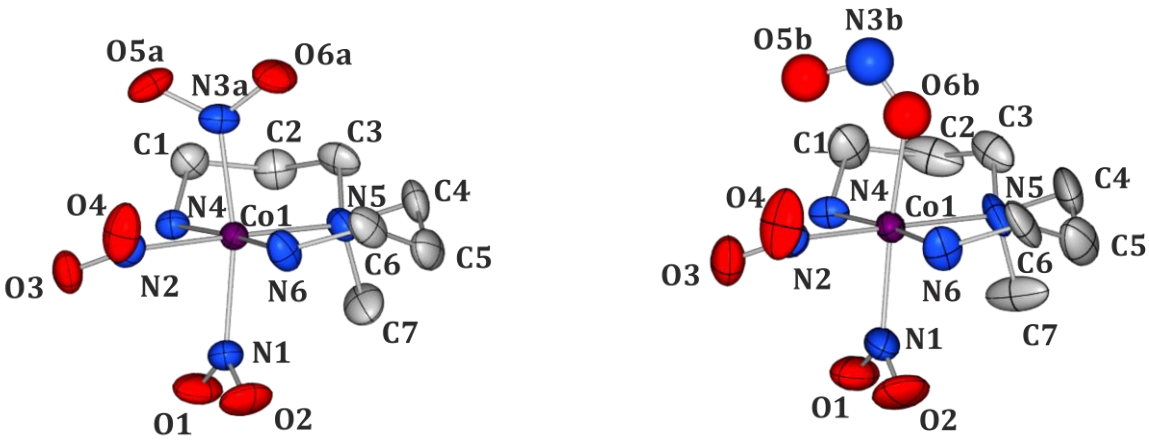

(*a*) (*b*)

Figure 1S. Deconvolution of the two isomers present in the room-temperature crystal structure of the [Co(Me-dpt)(NO_2)$_3$] complex (ellipsoids at the 30% probability level, H-atoms omitted for clarity): nitro isomer (*a*) and *endo*-nitrito isomer (*b*).

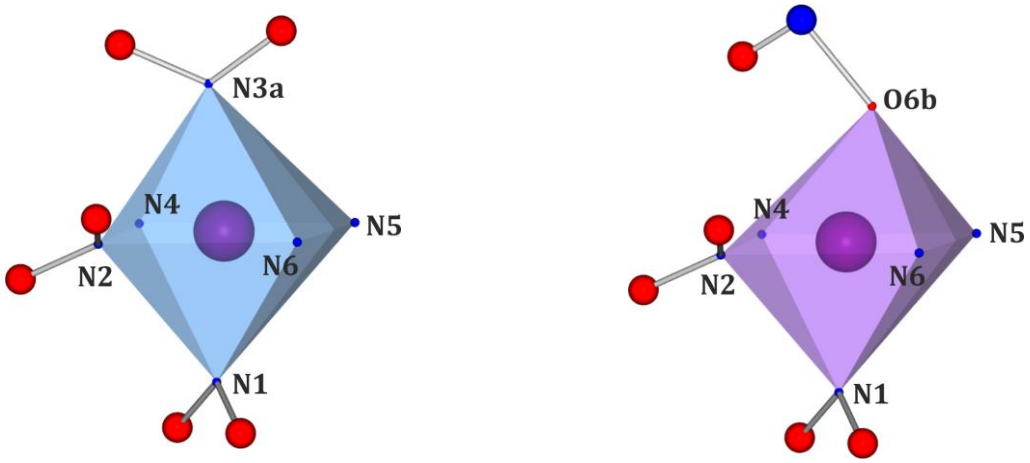

(*a*) (*b*)

Figure 2S. Polyhedra of cobalt coordination spheres generated for the nitro (*a*) and *endo*-nitrito (*b*) isomers in the in the room-temperature crystal structure of the [Co(Me-dpt)(NO2)$_3$] complex. The nitro isomer forms approximately tetragonal bipyramid; the *endo*-nitrito isomer coordination sphere follows the same pattern but it is more distorted in the upper part (O6b atom vertex leans towards the N6 and N5 nitrogen atoms).

Table 3S. Selected bond distances (all in Å) in the coordination sphere of the cobalt centre in the [Co(Me-dpt)$(NO_2)_3$] complex before and after irradiations. Data set codes are the same as in Table 2S.

Bond	*Data set*		
	RT-dark	**RT-irr470nm-1stRUN**	**RT-irr660nm-1stRUN**
Co1–N1	1.967(8)	1.960(9)	1.966(9)
Co1–N2	1.952(8)	1.942(9)	1.972(9)
Co1–N3a [a]	1.940(11)	1.92(2)	1.92(2)
Co1–O6b [b]	1.97(11)	1.94(3)	1.98(9)
Co1–N4	2.013(10)	1.983(10)	1.966(9)
Co1–N5	2.098(7)	2.111(8)	2.123(8)
Co1–N6	1.928(11)	1.975(10)	1.980(10)

[a] Only for nitro form. [b] Only for endo-nitrito form.

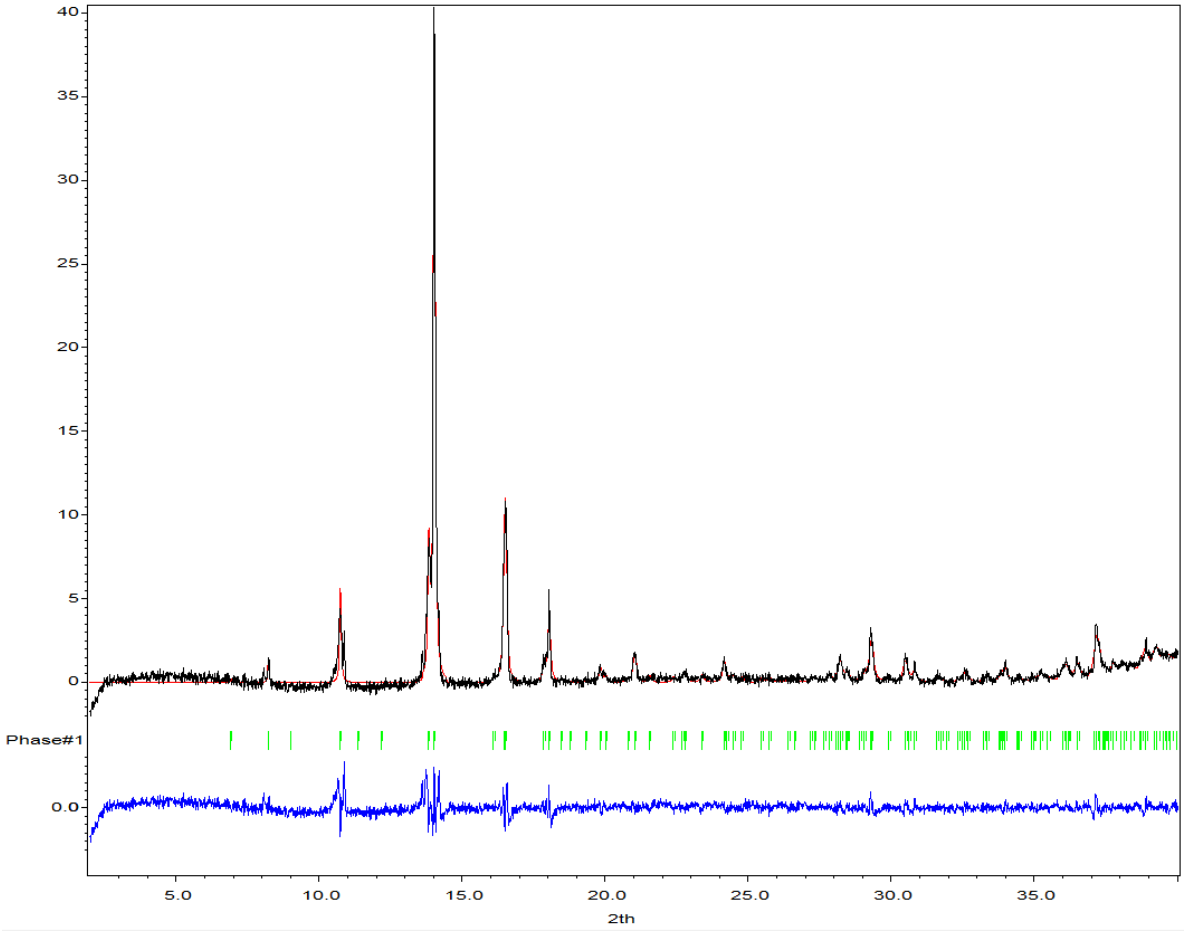

Figure 3S. PXRD pattern obtained for the bulk sample. Black curve – experimental pattern (with background subtracted), red – Le Bail-fitted model, green bars – reflection positions (taking into account the $K_{\alpha 1}$-$K_{\alpha 2}$ splitting), blue – residual.

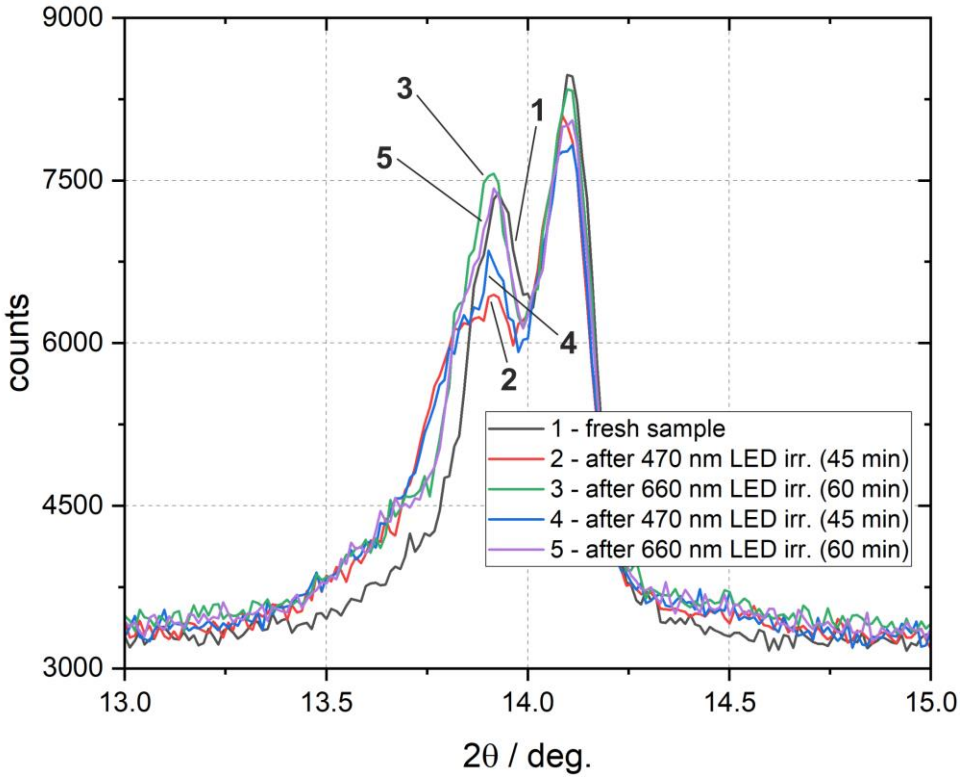

Figure 4S. PXRD results coupled with the LED irradiation. One can observe regular changes of the largest (split) peak intensity with no noticeable shifts of the peaks' positions. Peak intensity decreases after 470 nm LED irradiation, and recovers when sample is exposed to 660 nm LED light..

Table 4S. Summary of selected most important examples of photoswitchable transition-metal nitro complexes reported to date.

Compound	*Irradiation wavelength*	*Irradiation temperature*	*Temperature of reversion to the ground state*	*Conversion observed*
[Ni(dppe)(η^1-NO_2)]Cl[30]	400 nm	100 K	160 K	100%
Ni(Et_4dien)(NO_2)$_2$[31]	400 nm	100 K	160 K	86%
Ni(Me-dpt)(NO_2)(η^2-ONO)[32]	400 nm	100 K	150 K	89% / 32% [d]
Ni(η^5-C_5H_5)(IMes)(η^1-NO_2)[33]	470 nm	145 K	< 190 K	86% / 93% [d]
QTNiNO_2 (Ni complex [a])[34]	660 nm	160 K	240 K	100% [e] / 24% [f]
[Pd(Bu_4dien)(η^1-NO_2)]BPh_4[35]	400 nm	100 K	240 K / 260 K [c]	100%
[Pt(L)(NO_2)]PF_6[36]	365 nm	180 K	180 K	81%
[Pt(PCy_3)$_2$(NO_2)$_2$][37]	400 nm	300 K	300 K	27%
Cu-2a (Cu complex [a,b])[38]	590 nm	10 K	60 K	– [g]
Cu-2b (Cu complex [a,b])[38]	405 nm	10 K	80 K	– [g]

[a] Abbreviation as used in the original publication. [b] Ground-state isomer for this compound is κ-nitrito. [c] Under continuous illumination. [b] Two values given for molecules A and B (symmetry-independent molecules in the asymmetric unit). [c] Value obtained from IR measurements. [d] Value obtained with single-crystal XRD. [g] Value not given. Estimated to be low.

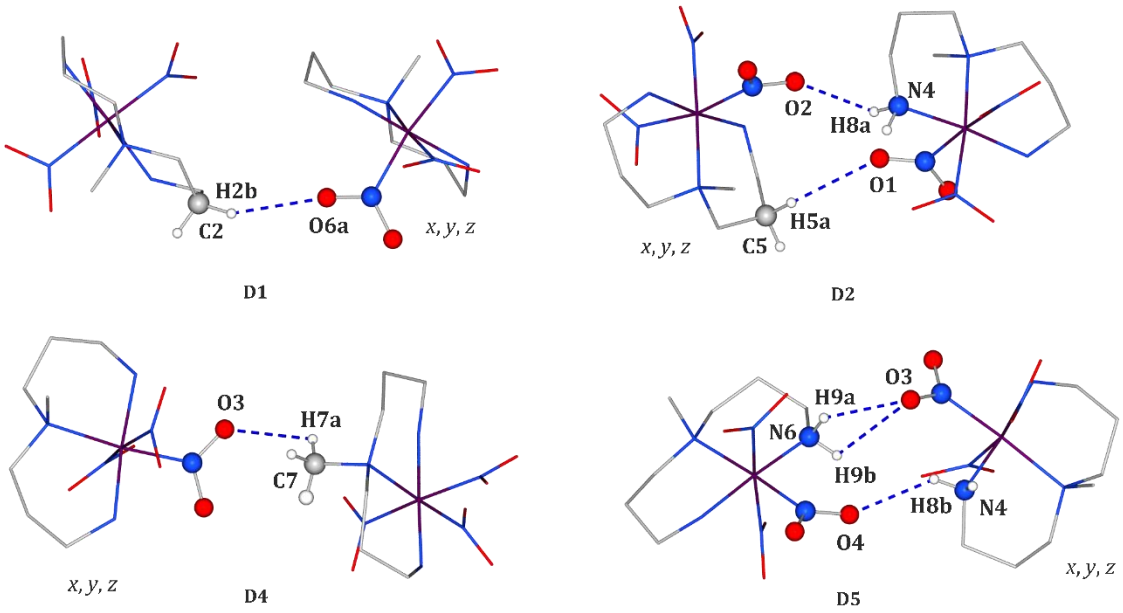

Figure 5S. Schematic representation of selected structural dimeric ground-state–ground-state (GS-GS) motifs encountered in the [Co(Me-dpt)$(NO_2)_3$] crystal structure. Note one molecule is always of an *x*, *y*, *z* symmetry. For interaction energies see Table 5S.

Table 5S. Selected ground-state–ground-state (GS-GS) dimeric motifs present in the examined crystal structure (see Figure 5S for visualization): geometrical parameters and interaction energy values (E_{int}; DFT(B3LYP)/6-311++G** level of theory with the Grimme dispersion correction applied; geometries with the X–H neutron-normalized distances were used for computations). Note one molecule is always of an *x*, *y*, *z* symmetry.

Motif	E_{int} / kJ·mol^{-1}	*Selected interactions*	d_{D-H} / Å	$d_{H\cdots A}$ / Å	$d_{D\cdots A}$ / Å	$\theta_{D-H\cdots A}$ / °
D1	−44.80	O6a···H2b$^{\#1}$–C2$^{\#1}$	0.96	2.58	3.376(15)	140.15
D2	−62.47	O1$^{\#2}$···H5a–C5	0.96	2.61	3.345(13)	134.15
		O2···H8a$^{\#2}$–N4$^{\#2}$	0.87	2.30	3.030(12)	141.01
D4	−14.40	O3···H7a$^{\#4}$–C7$^{\#4}$	0.96	2.72	3.305(15)	120.21
D5	−65.65	O4$^{\#5}$···H8b–N4	0.87	2.41	3.105(12)	137.74
		O3···H9a$^{\#5}$–N6$^{\#5}$	0.87	2.64	3.034(13)	108.41
		O3···H9b$^{\#5}$–N6$^{\#5}$	0.87	2.37	3.034(13)	132.87
Symmetry operations: (#1) $-x+1, -y, z-0.5$, (#2) $-x, -y-1, z-0.5$, (#4) $x-0.5, -y+1, z$ (#5) $-x+0.5, y, z+0.5$.						

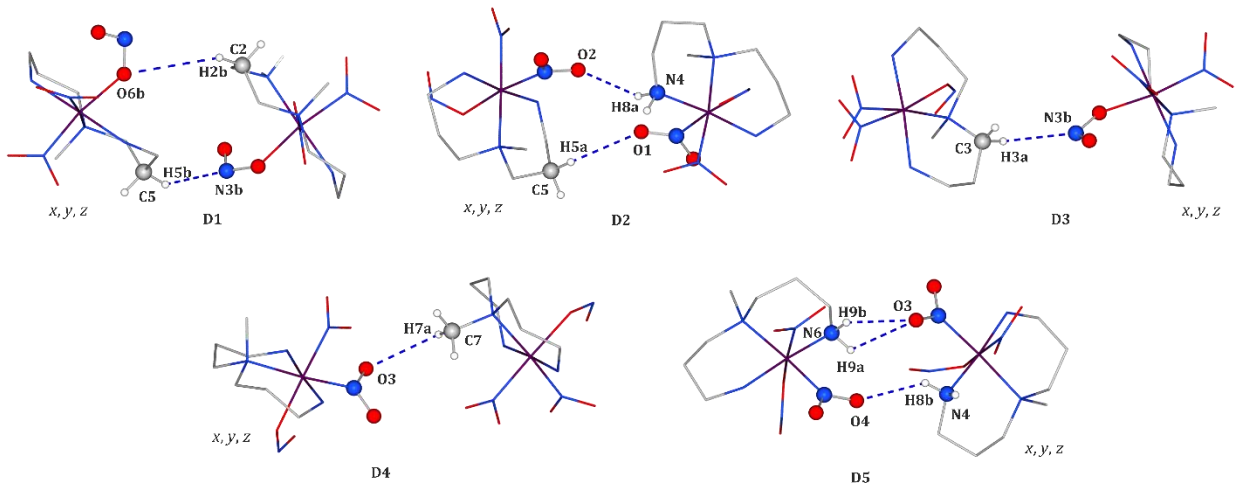

Figure 6S. Schematic representation of selected structural dimeric metastable-state–metastable-state (MS3-MS3) motifs encountered in the [Co(Me-dpt)$(NO_2)_3$] crystal structure (MS3 – molecule with the photoactive O5–N3–O6 group in the nitrito form). Note one molecule is always of an *x*, *y*, *z* symmetry. For interactions energies see Table 6S.

Table 6S. Selected metastable-state–metastable-state (MS3-MS3) dimeric motifs present in the examined crystal structure (see Figure 6S for visualization): geometrical parameters and interaction energy values (E_{int}; DFT(B3LYP)/6-311++G** level of theory with the Grimme dispersion correction applied; geometries with the X–H neutron-normalized distances were used for computations). Note one molecule is always of an *x*, *y*, *z* symmetry.

Motif	E_{int} / kJ·mol^{-1}	*Selected interactions*	d_{D-H} / Å	$d_{H\cdots A}$ / Å	$d_{D\cdots A}$ / Å	$\theta_{D-H\cdots A}$ / °
D1	−33.54	N3b$^{\#1}$···H5b–C5	0.96	2.52	3.34(10)	143.37
		O6b···H2b$^{\#1}$–C2$^{\#1}$	0.96	2.58	3.376(15)	140.15
D2	−61.00	O1$^{\#2}$···H5a–C5	0.96	2.61	3.345(13)	134.15
		O2···H8a$^{\#2}$–N4$^{\#2}$	0.87	2.30	3.030(12)	141.01
D3	−15.70	N3b···H3a$^{\#3}$–C3$^{\#3}$	0.96	2.67	3.57(10)	156.24
D4	−14.15	O3···H7a$^{\#4}$–C7$^{\#4}$	0.96	2.72	3.305(15)	120.21
D5	−61.17	O4$^{\#5}$···H8b–N4	0.87	2.41	3.105(12)	137.74
		O3···H9a$^{\#5}$–N6$^{\#5}$	0.87	2.64	3.034(13)	108.41
		O3···H9b$^{\#5}$–N6$^{\#5}$	0.87	2.37	3.034(13)	132.87

Symmetry operations: (#1) $-x+1, -y, z-0.5$, (#2) $-x, -y-1, z-0.5$, (#3) $x-0.5, -y, z$, (#4) $x-0.5, -y+1, z$, (#5) $-x+0.5, y, z+0.5$.

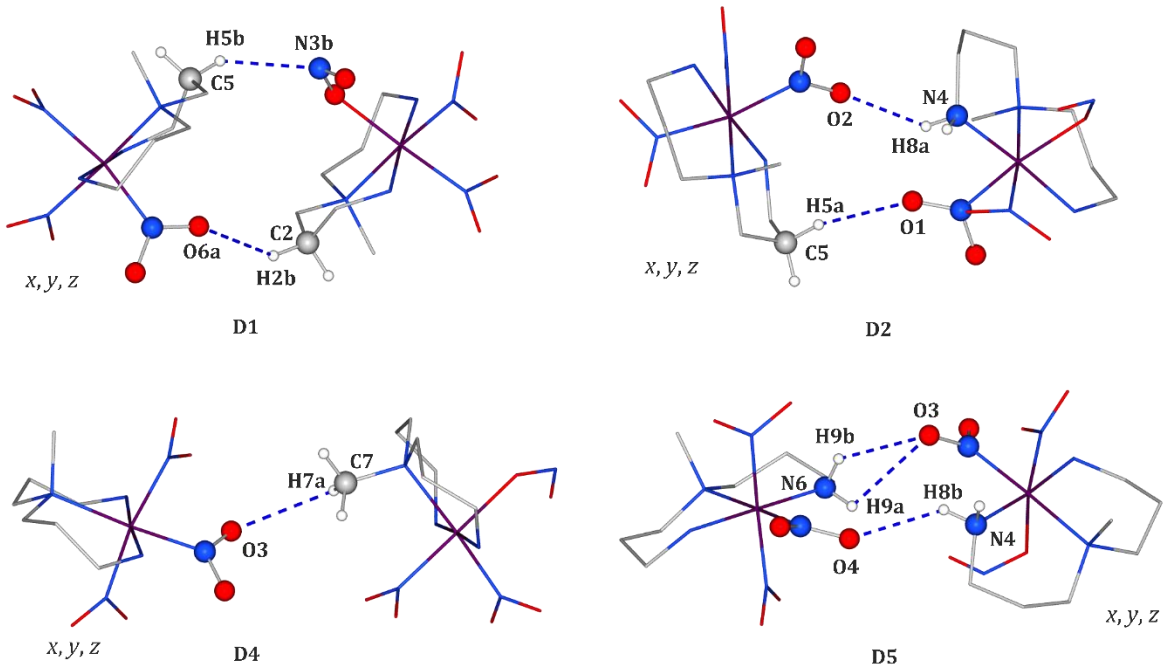

Figure 7S. Schematic representation of selected structural dimeric ground-state–metastable-state (GS-MS3) motifs encountered in the [Co(Me-dpt)$(NO_2)_3$] crystal structure. Note one molecule is always of an *x*, *y*, *z* symmetry. For interactions energies see Table 7S.

Table 7S. Selected ground-state–metastable-state (GS-MS3) dimeric motifs present in the examined crystal structure (see Figure 7S for visualization): geometrical parameters and interaction energy values (E_{int}; DFT(B3LYP)/6-311++G** level of theory with the Grimme dispersion correction applied; geometries with the X–H neutron-normalized distances were used for computations). Note one molecule is always of an *x*, *y*, *z* symmetry.

Motif	E_{int} / kJ·mol^{-1}	*Selected interactions*	d_{D-H} / Å	$d_{H\cdots A}$ / Å	$d_{D\cdots A}$ / Å	$\theta_{D-H\cdots A}$ / °
D1	−37.39	O6a···H2b$^{\#1}$–C2$^{\#1}$	0.96	2.58	3.376(15)	140.15
		N3b$^{\#1}$···H5b–C5	0.96	2.52	3.34(10)	143.37
D2	−61.92	O1$^{\#2}$···H5a–C5	0.96	2.61	3.345(13)	134.15
		O2···H8a$^{\#2}$–N4$^{\#2}$	0.87	2.30	3.030(12)	141.01
D4	−15.41	O3···H7a$^{\#4}$–C7$^{\#4}$	0.96	2.72	3.305(15)	120.21
D5	−63.60	O4$^{\#5}$···H8b–N4	0.87	2.41	3.105(12)	137.74
		O3···H9a$^{\#5}$–N6$^{\#5}$	0.87	2.64	3.034(13)	108.41
		O3···H9b$^{\#5}$–N6$^{\#5}$	0.87	2.37	3.034(13)	132.87

Symmetry operations: (#1) $-x+1, -y, z-0.5$, (#2) $-x, -y-1, z-0.5$, (#4) $x-0.5, -y+1, z$, (#5) $-x+0.5, y, z+0.5$.

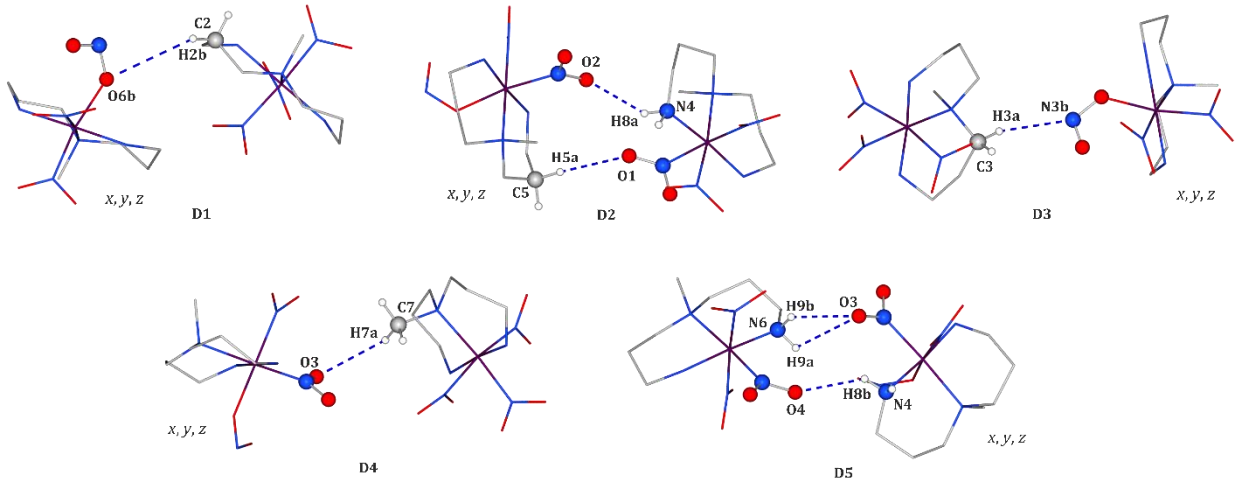

Figure 8S. Schematic representation of selected structural dimeric metastable-state–ground-state (MS3-GS) motifs encountered in [Co(Me-dpt)$(NO_2)_3$] crystal structure. Note one molecule is always of an *x*, *y*, *z* symmetry. For interactions energies see Table 8S.

Table 8S. Selected metastable-state–ground-state (MS-GS) dimeric motifs present in the examined crystal structure (see Figure 8S for visualization): geometrical parameters and interaction energy values (E_{int}; DFT(B3LYP)/6-311++G** level of theory with the Grimme dispersion correction applied; geometries with the X–H neutron-normalized distances were used for computations). Note one molecule is always of an *x*, *y*, *z* symmetry.

Motif	E_{int} / kJ·mol^{-1}	*Selected interactions*	d_{D-H} / Å	$d_{H\cdots A}$ / Å	$d_{D\cdots A}$ / Å	$\theta_{D-H\cdots A}$ / °
D1	−40.61	O6b···H2b$^{\#1}$–C2$^{\#1}$	0.96	2.58	3.376(15)	140.15
D2	−62.30	O1$^{\#2}$···H5a–C5	0.96	2.61	3.345(13)	134.15
		O2···H8a$^{\#2}$–N4$^{\#2}$	0.87	2.30	3.030(12)	141.01
D3	−15.66	N3b···H3a$^{\#3}$–C3$^{\#3}$	0.96	2.67	3.57(10)	156.24
D4	−15.49	O3···H7a$^{\#4}$–C7$^{\#4}$	0.96	2.72	3.305(15)	120.21
D5	−63.47	O4$^{\#5}$···H8b–N4	0.87	2.41	3.105(12)	137.74
		O3···H9a$^{\#5}$–N6$^{\#5}$	0.87	2.64	3.034(13)	108.41
		O3···H9b$^{\#5}$–N6$^{\#5}$	0.87	2.37	3.034(13)	132.87
Symmetry operations: (#1) −*x*+1, −*y*, *z*−0.5, (#2) −*x*, −*y*−1, *z*−0.5, (#4) *x*−0.5, −*y*+1, *z* (#5) −*x*+0.5, *y*, *z*+0.5.						

Table 9S. The reaction-cavity volumes given per one complex molecule calculated for the [Co(Me-dpt)(NO_2)$_3$] crystal structure, before and after irradiation, for all three distinct NO_2 groups. Cavity volumes were computed with the *MERCURY* program[39] (probe radius of 1.2 Å, grid spacing of 0.1 Å).

NO_2 group	*Before irradiation*	*After irradiation*
O1–N1–O2	22.24	21.22
O3–N2–O4	24.90	27.69
O5–N3–O6	29.57	31.83

Table 10S. Relative molecular energies (E_{rel}) calculated with respect to the ground-state form at the DFT(B3LYP)/6-311++G** level of theory for the examined isomers optimised as isolated molecules or using the QM/MM method (values in square brackets are zero-point-energy corrected). GS – ground state, MS1 – molecule with the O1–N1–O2 group in the nitrito form, MS2 – molecule with the O3–N2–O4 group in the nitrito form, MS3 – molecule with the O5–N3–O6 group in the nitrito form.

Form	*QM/MM*	*Isolated molecule*
	E_{rel} / kJ·mol^{-1}	E_{rel} / kJ·mol^{-1}
GS	0.0	0.0
MS1	+32.8	+20.7 [+16.9]
MS2	+41.8	+21.9 [+18.8]
MS3	+54.3 [+51.3]	+5.1 [+1.4]

Table 11S. Comparison of interaction energies (E_{int}; DFT(B3LYP)/6-311++G** level of theory with the Grimme dispersion correction applied) between molecules forming major structural dimeric motifs. The symmetry code of the first molecule in a dimer (*e.g.* GS-MS3) is always x, y, z.

Motif	GS-GS	MS3-MS3	GS-MS3	MS3-GS
	E_{int} / kJ·mol^{-1}	E_{int} / kJ·mol^{-1}	E_{int} / kJ·mol^{-1}	E_{int} / kJ·mol^{-1}
D1[#1]	−44.80	−33.54	−37.39	−40.61
D2[#2]	−62.47	−61.00	−61.92	−62.30
D3[#3]	—	−15.70	—	−15.66
D4[#4]	−14.40	−14.15	−15.41	−15.49
D5[#5]	−65.65	−61.17	−63.60	−63.47
Symmetry operations: (#1) $-x+1, -y, z-0.5$, (#2) $-x, -y-1, z-0.5$, (#3) $x-0.5, -y, z$, (#4) $x-0.5, -y+1, z$, (#5) $-x+0.5, y, z+0.5$.				

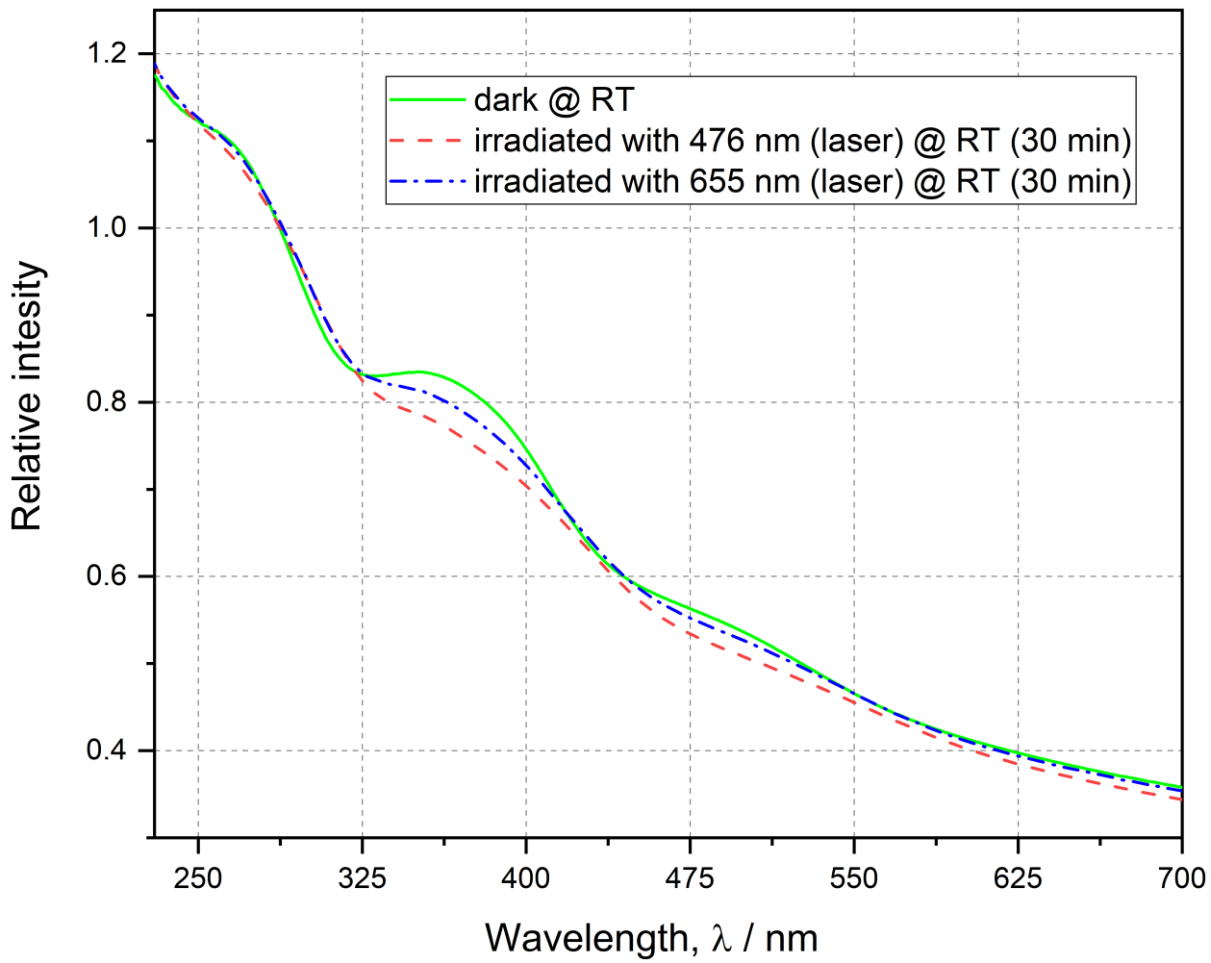

Figure 9S. Solid-state UV-Vis absorption spectra: green solid line – spectra without irradiation at room temperature; red dased line – spectra after irradiation with 476 nm laser light for 30 minutes at room temperature; blue dashed-dot line – spectra after irradiation with 655 nm laser light for 30 minutes at room temperature.

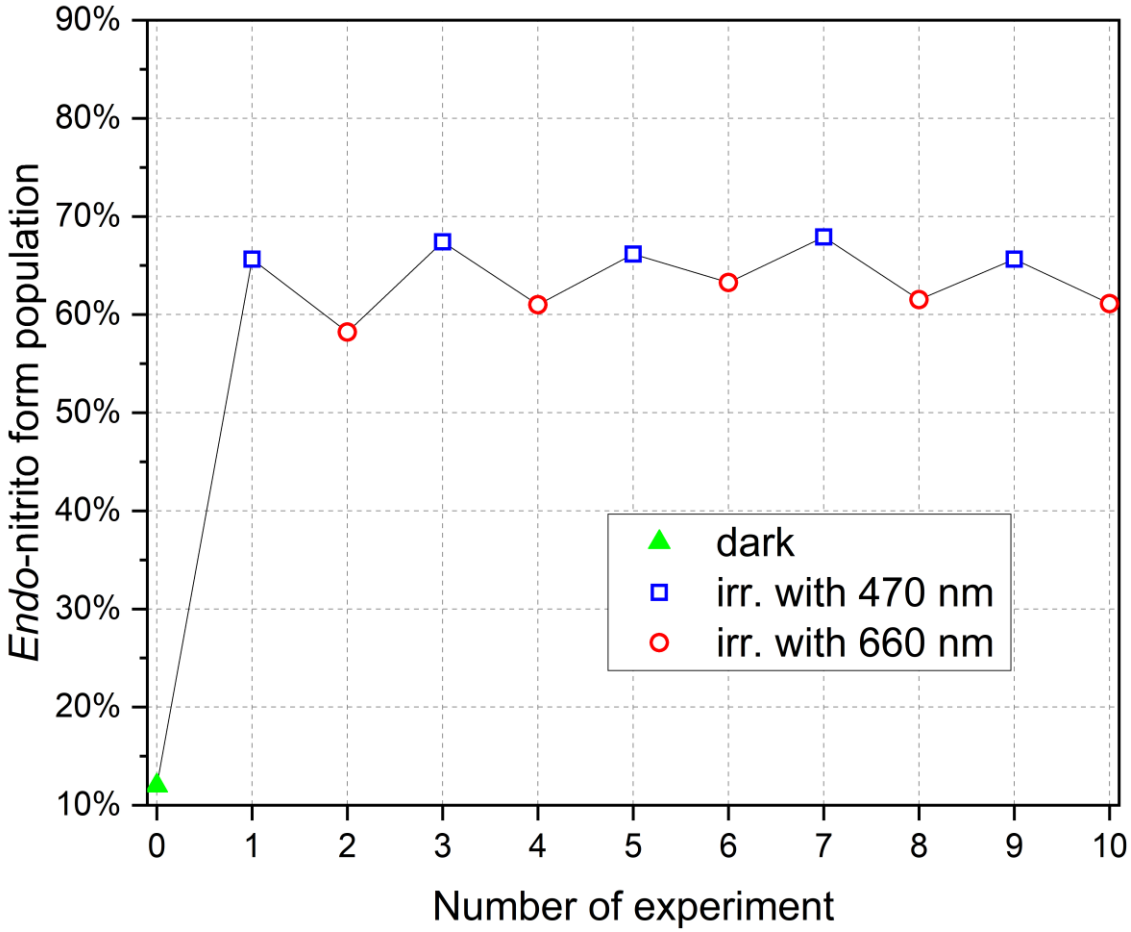

Figure 10S. Representation of the reversibility of the reaction after subsequent irradiations (green triangle – initial state with 12% of the nitrito form, blue squares – nitrito form populations after 470 nm LED irradiations, red circles – nitrito form populations after 660 nm LED irradiations). Populations are estimated based on the 781 cm^{-1} peak area. Experiment numbers are the same as in Table 2 in the main text.

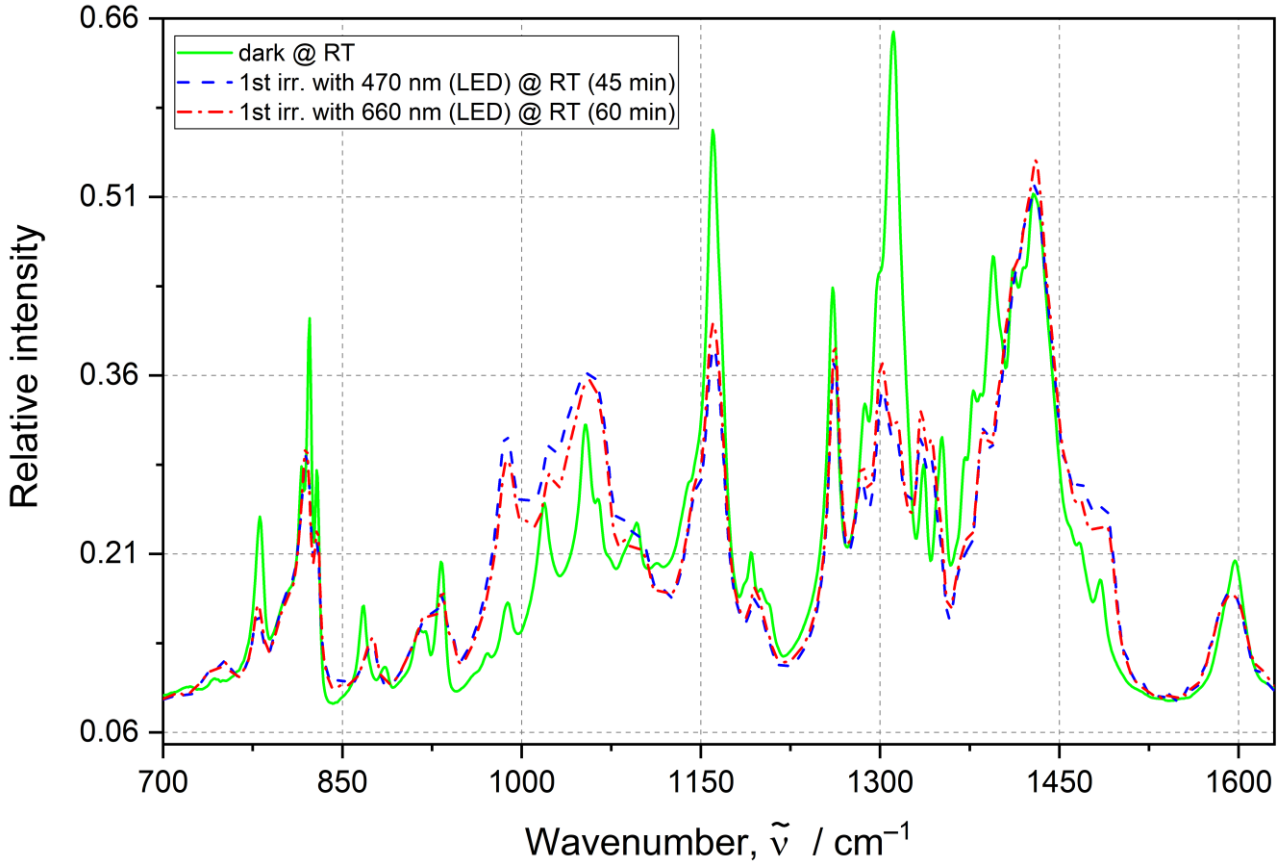

Figure 11S. IR absorption spectra collected for [Co(Me-dpt)$(NO_2)_3$] in the solid state for the initial sample, after the 1st cycle of 470 and 660 nm LED light irradiation.

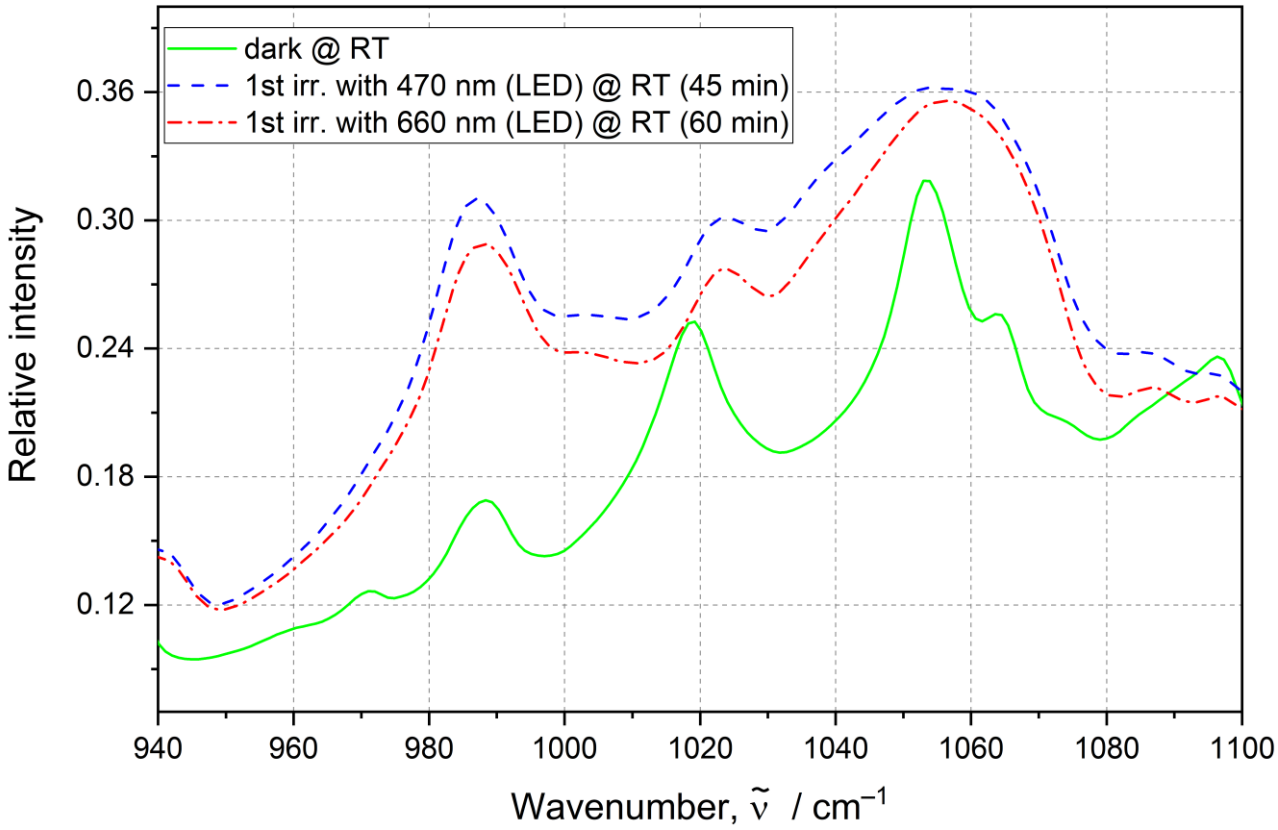

Figure 11S (continued). IR absorption spectra collected for [Co(Me-dpt)(NO_2)$_3$] in the solid state for the initial sample, after the 1st cycle of 470 and 660 nm LED light irradiation.

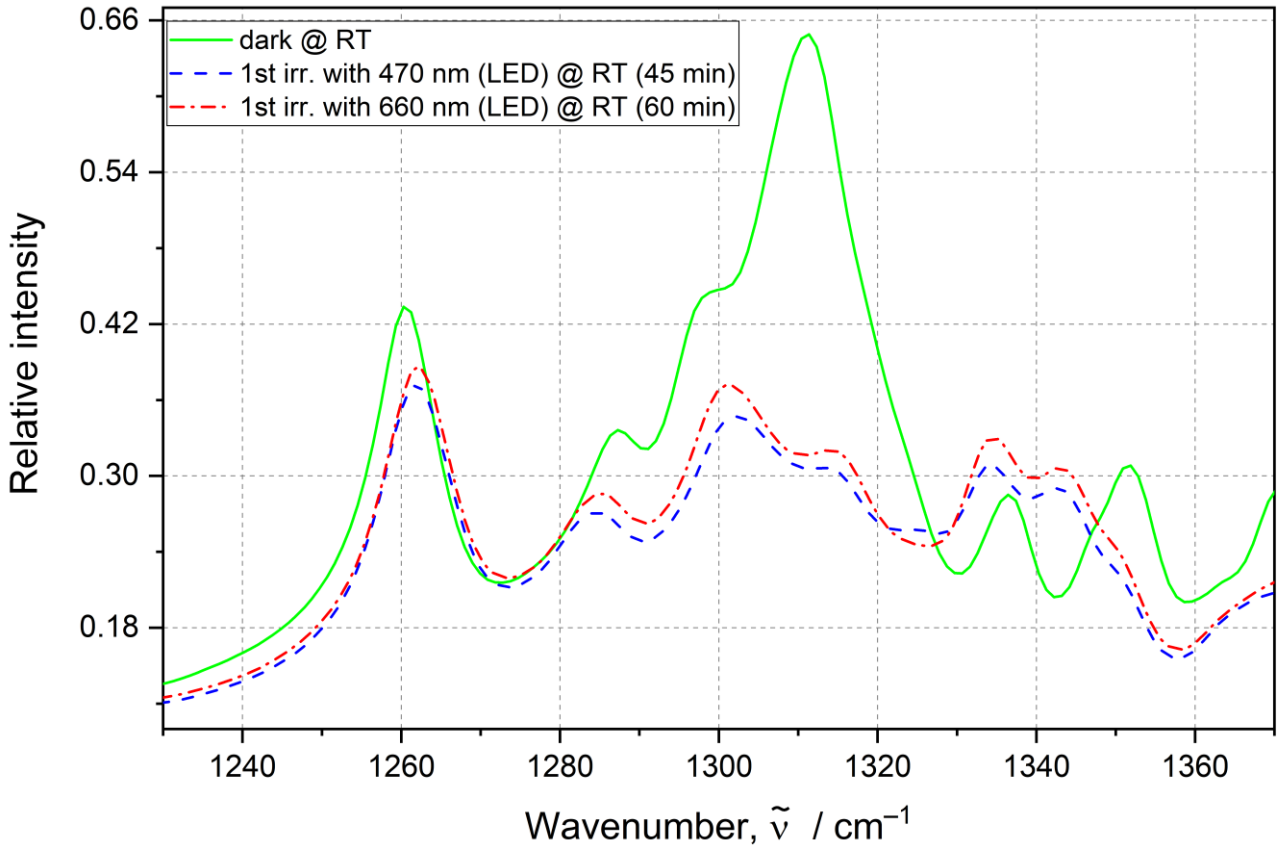

Figure 11S (continued). IR absorption spectra collected for [Co(Me-dpt)$(NO_2)_3$] in the solid state for the initial sample, after the 1st cycle of 470 and 660 nm LED light irradiation.

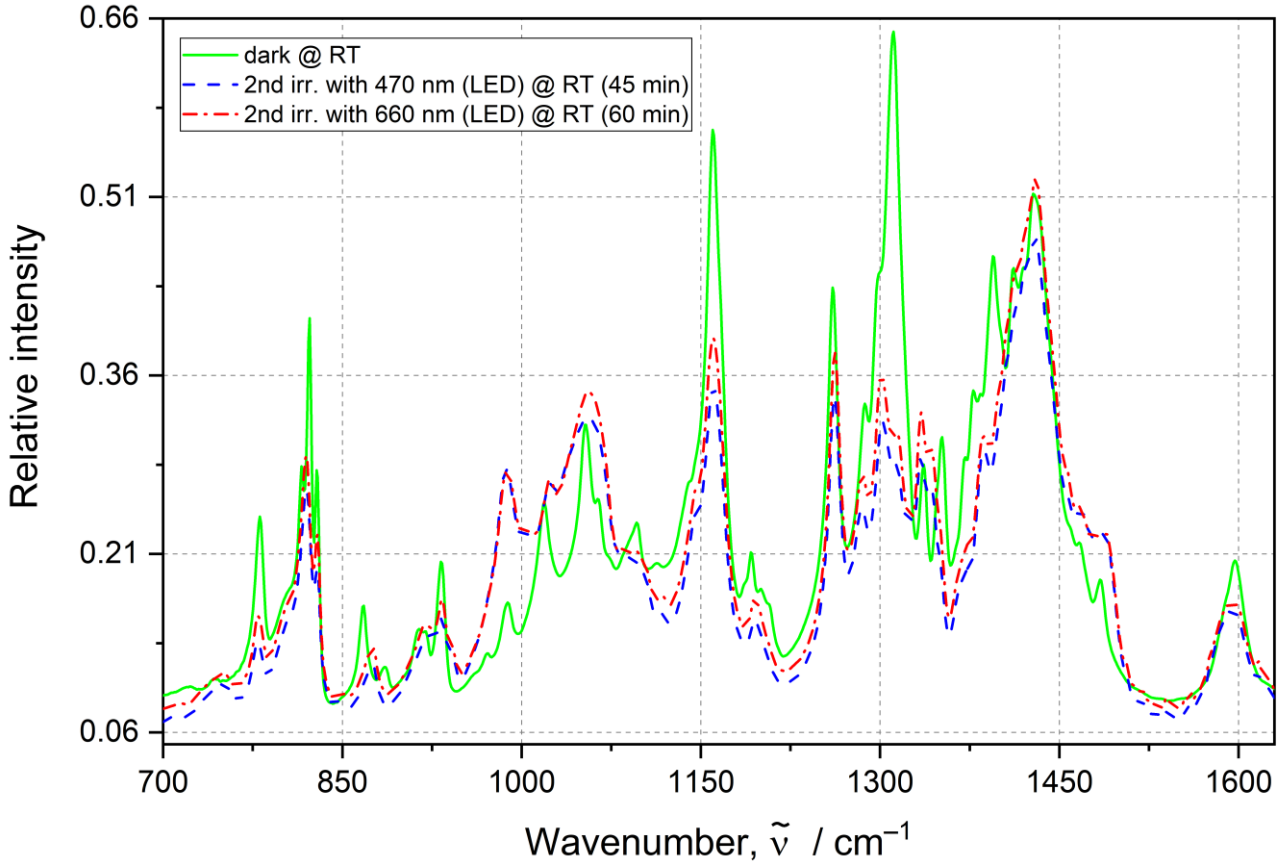

Figure 12S. IR absorption spectra collected for [Co(Me-dpt)$(NO_2)_3$] in the solid state for the initial sample, after the 2nd cycle of 470 and 660 nm laser LED irradiation.

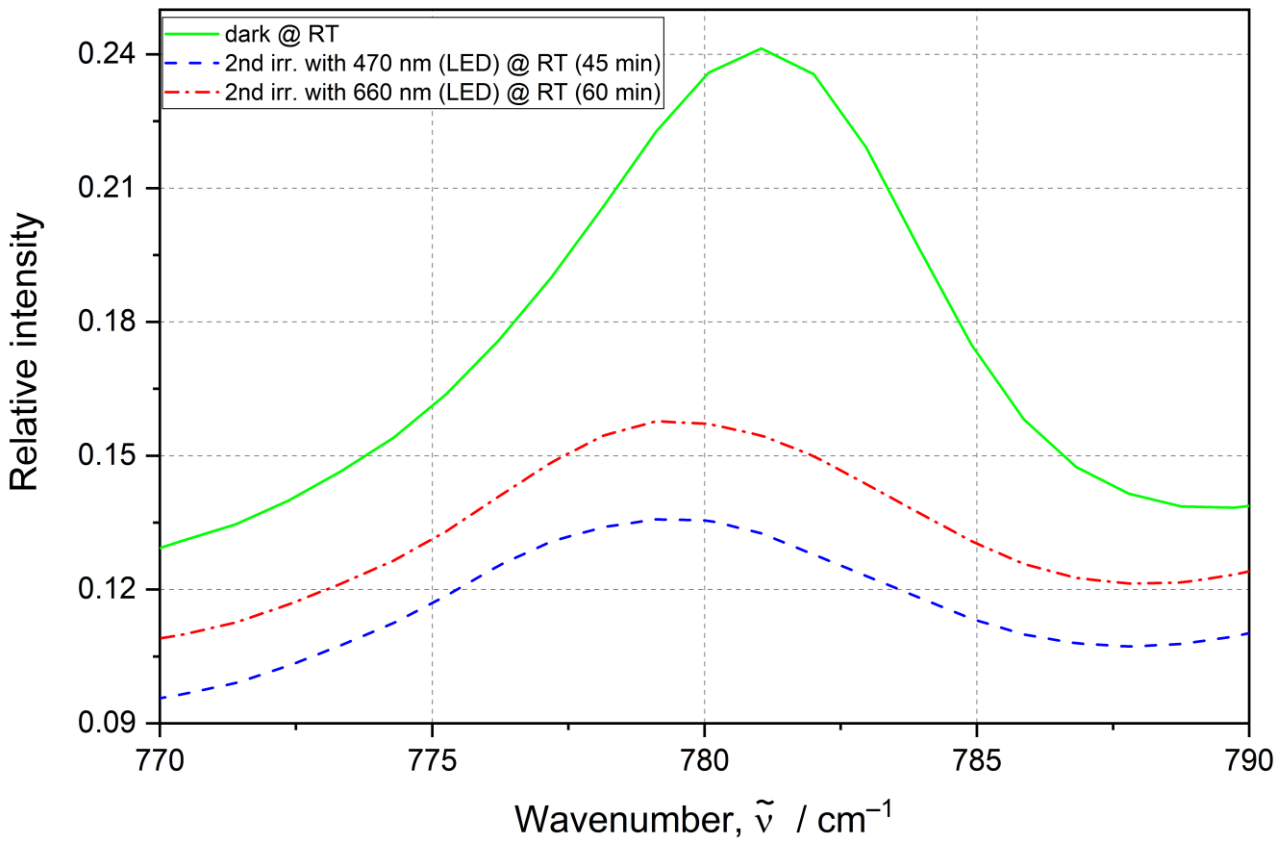

Figure 12S (continued). IR absorption spectra collected for [Co(Me-dpt)$(NO_2)_3$] in the solid state for the initial sample, after the 2nd cycle of 470 and 660 nm LED light irradiation.

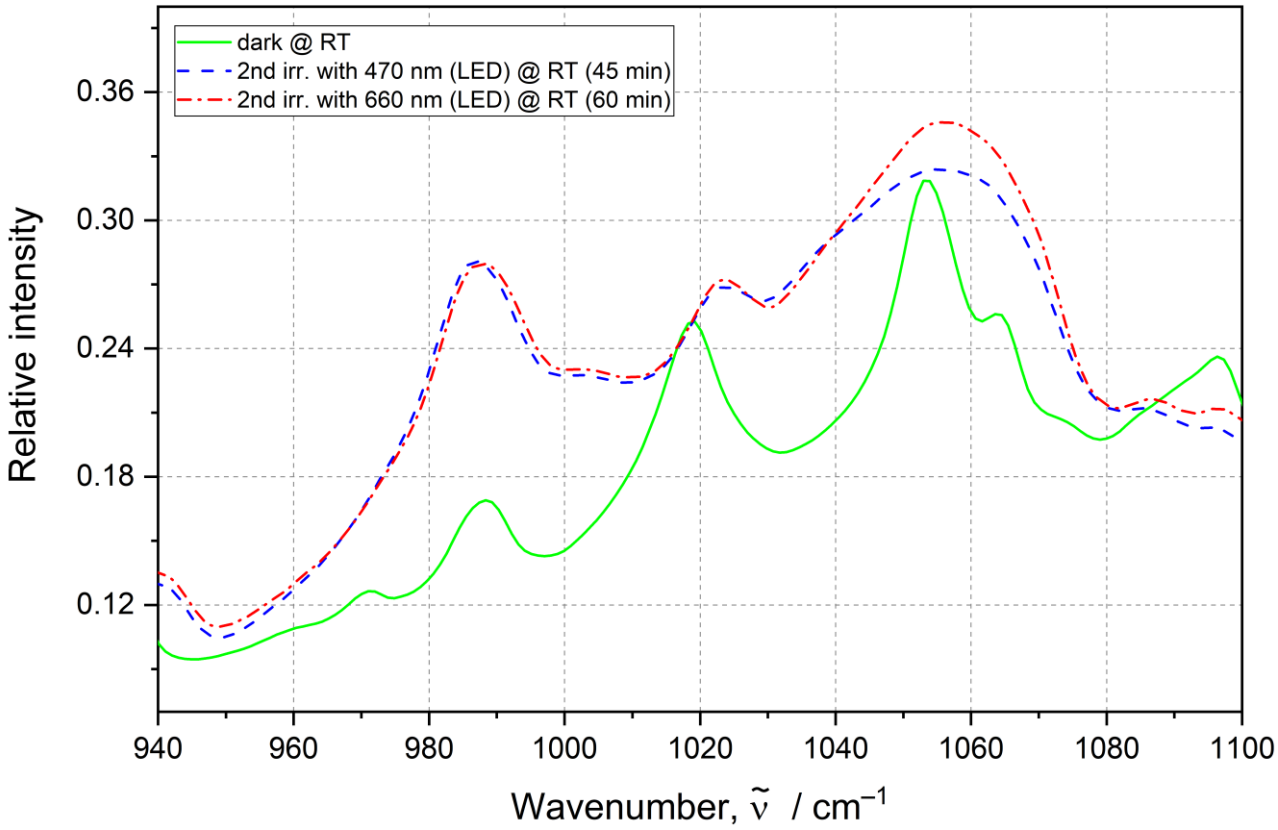

Figure 12S (continued). IR absorption spectra collected for [Co(Me-dpt)(NO_2)$_3$] in the solid state for the initial sample, after the 2nd cycle of 470 and 660 nm LED light irradiation.

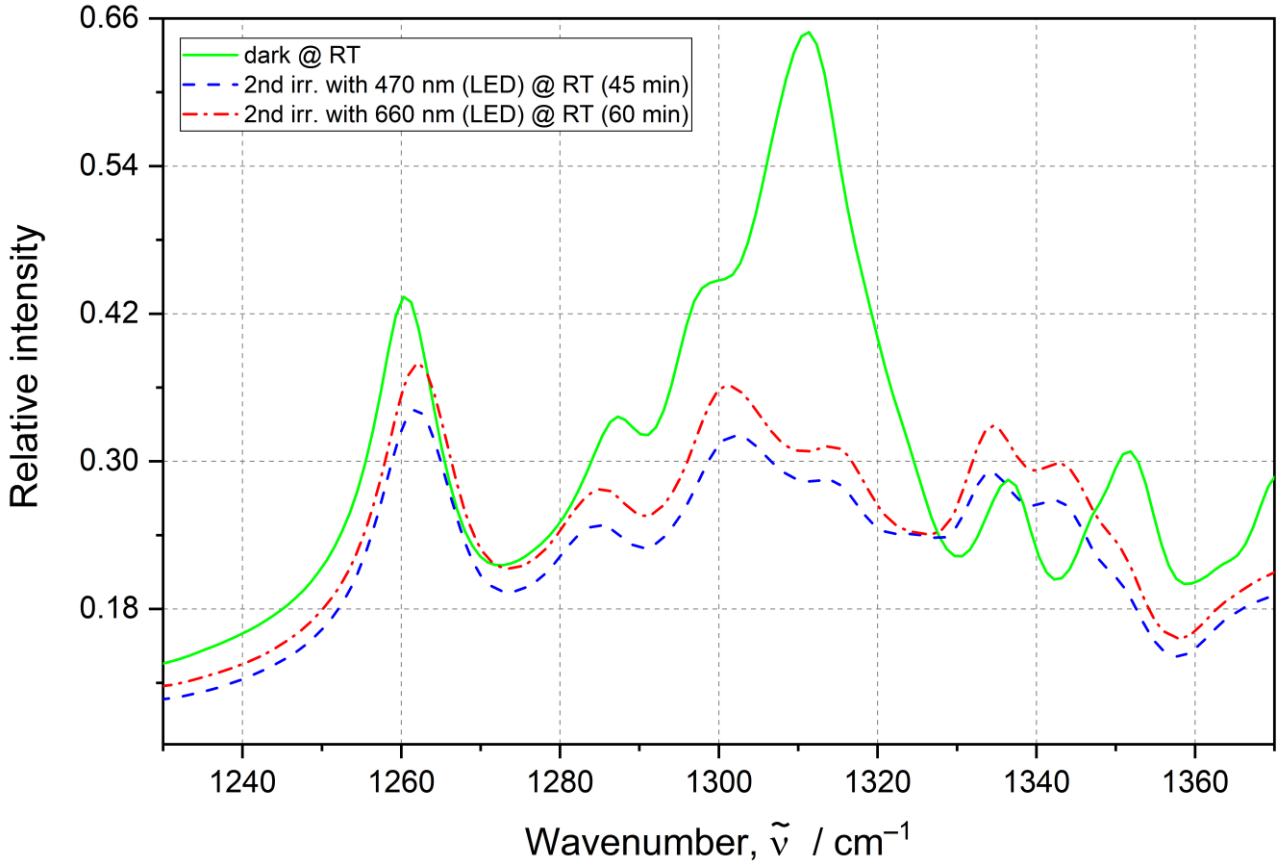

Figure 12S (continued). IR absorption spectra collected for [Co(Me-dpt)$(NO_2)_3$] in the solid state for the initial sample, after the 2nd cycle of 470 and 660 nm LED light irradiation.

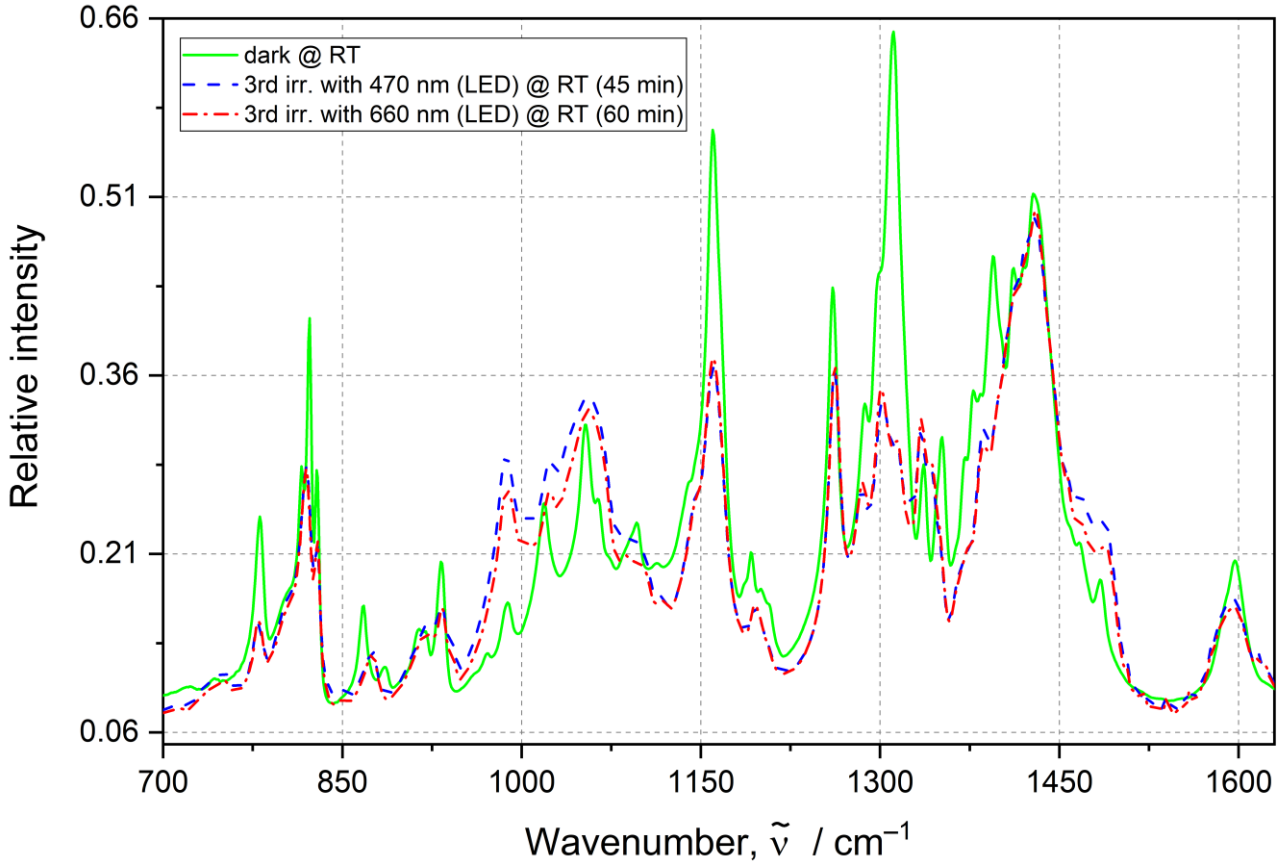

Figure 13S. IR absorption spectra collected for [Co(Me-dpt)$(NO_2)_3$] in the solid state for the initial sample, after the 3rd cycle of 470 and 660 nm LED light irradiation.

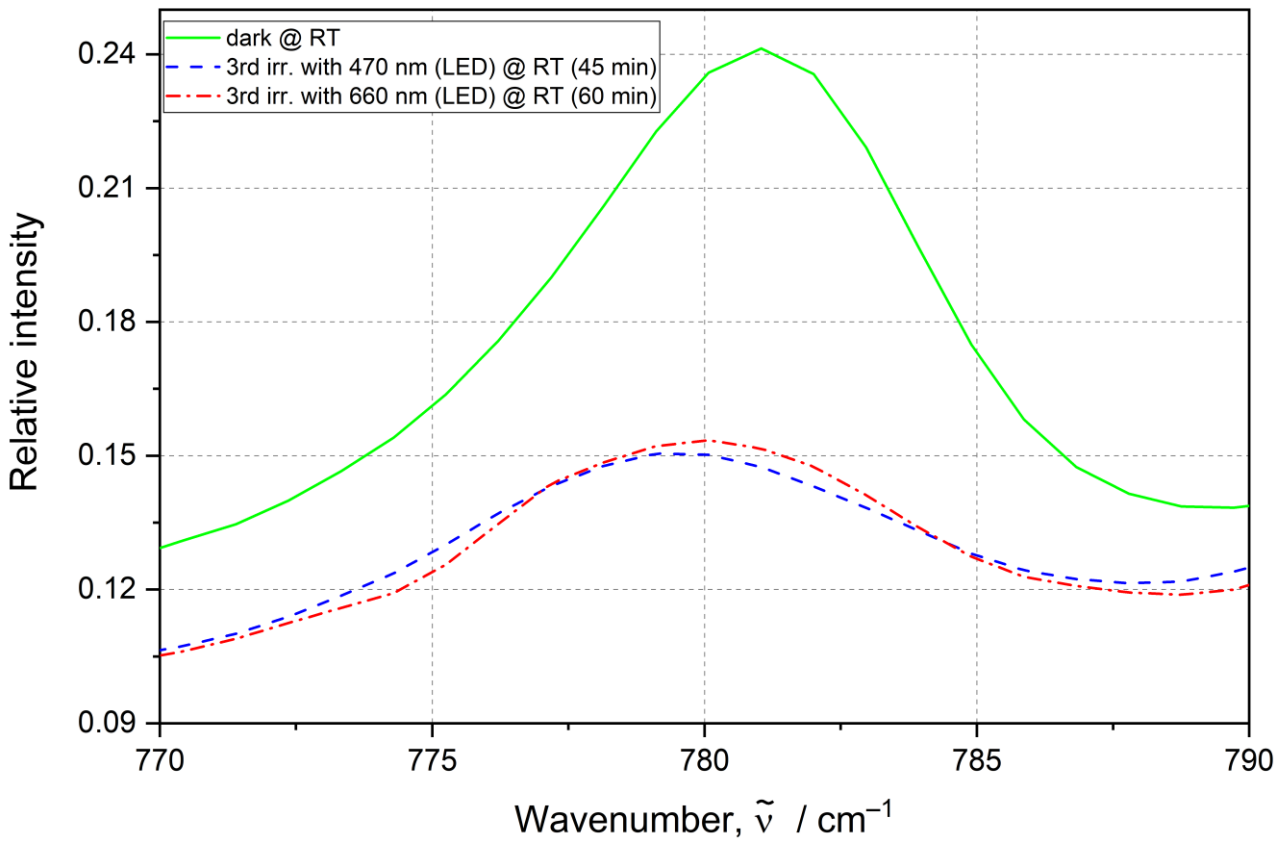

Figure 13S (continued). IR absorption spectra collected for [Co(Me-dpt)(NO_2)$_3$] in the solid state for the initial sample, after the 3rd cycle of 470 and 660 nm LED light irradiation.

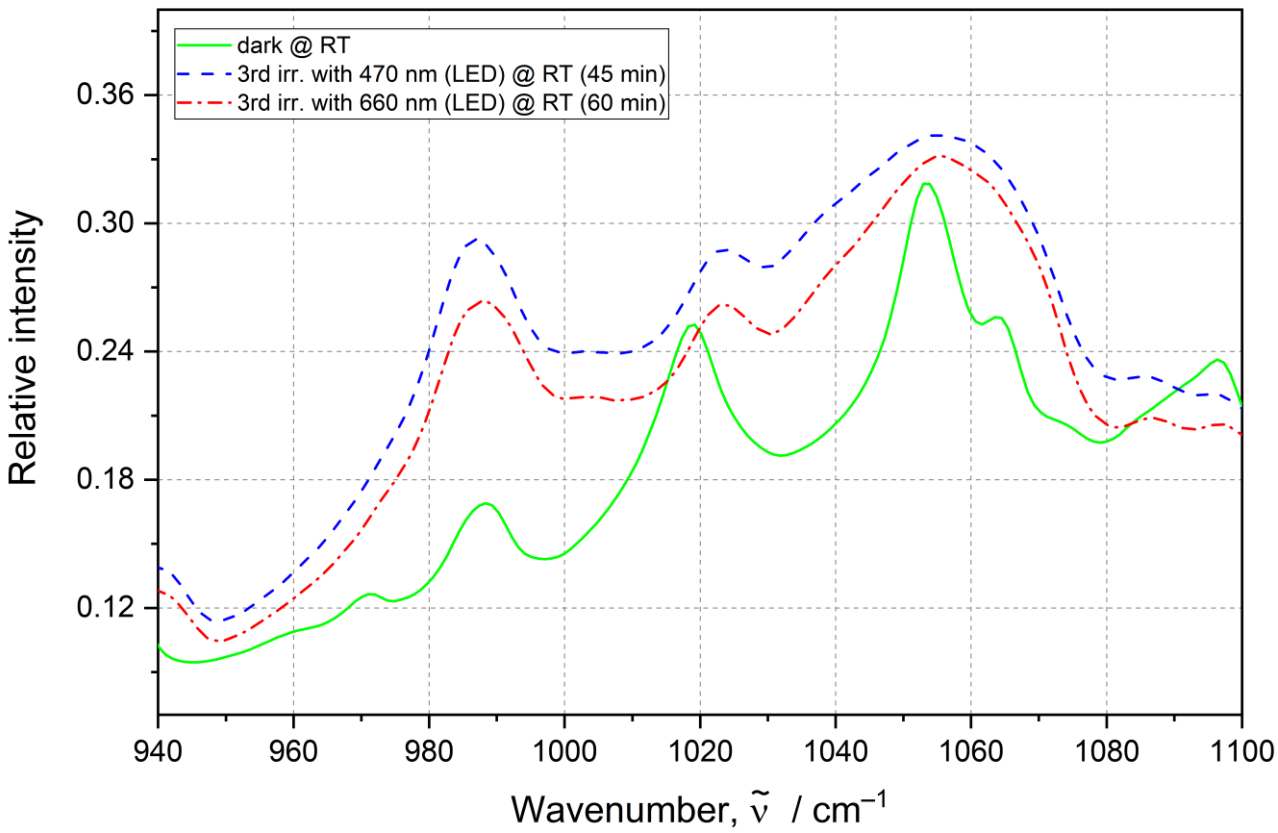

Figure 13S (continued). IR absorption spectra collected for [Co(Me-dpt)$(NO_2)_3$] in the solid state for the initial sample, after the 3rd cycle of 470 and 660 nm LED light irradiation.

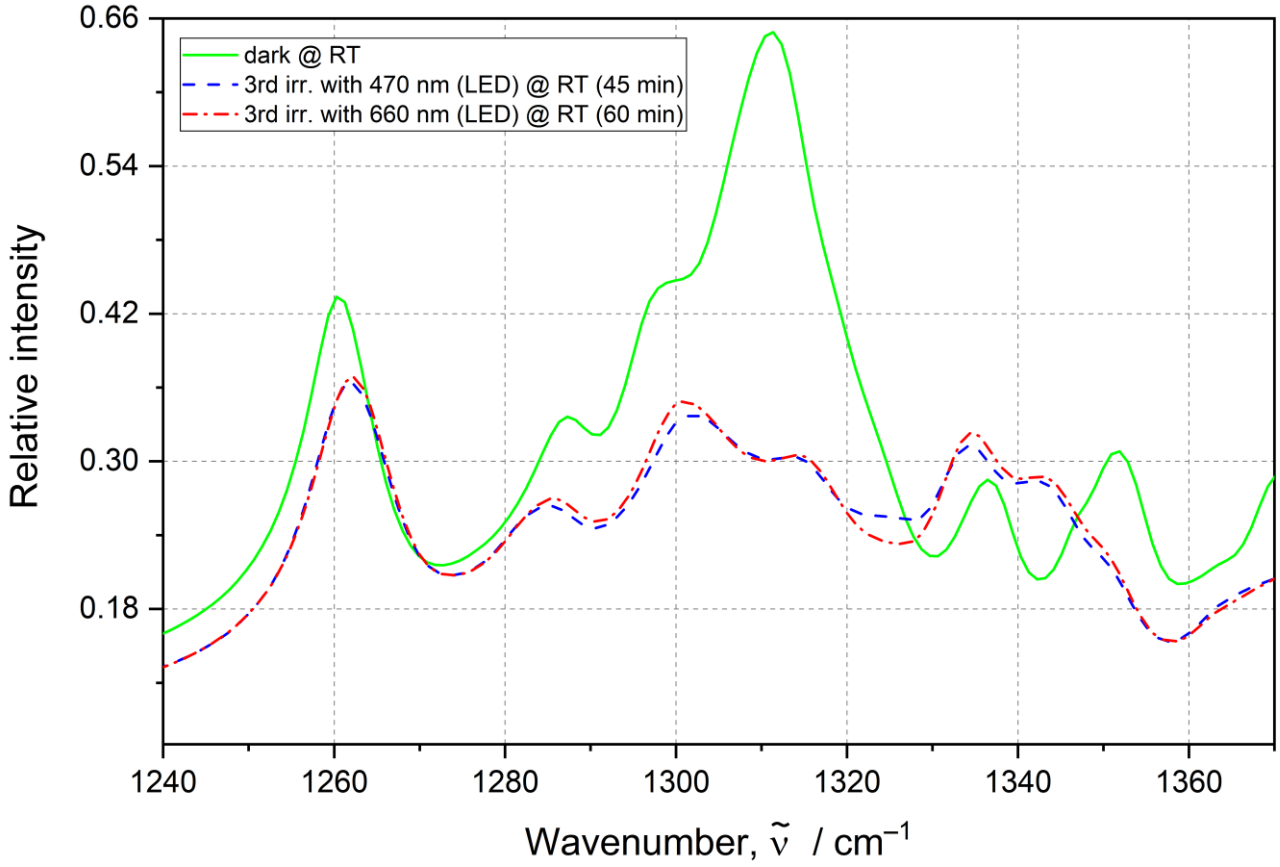

Figure 13S (continued). IR absorption spectra collected for [Co(Me-dpt)$(NO_2)_3$] in the solid state for the initial sample, after the 3rd cycle of 470 and 660 nm LED light irradiation.

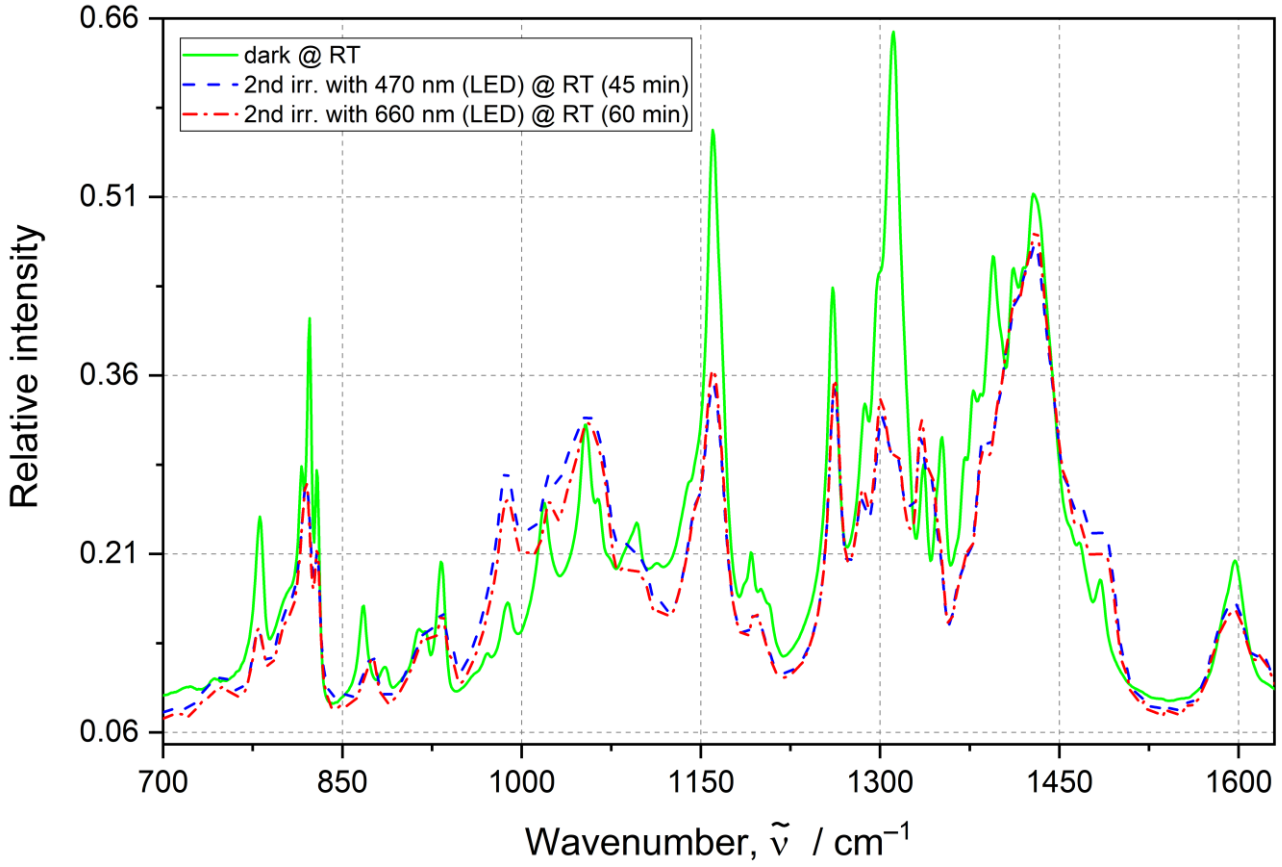

Figure 14S. IR absorption spectra collected for [Co(Me-dpt)$(NO_2)_3$] in the solid state for the initial sample, after the 4th cycle of 470 and 660 nm LED light irradiation.

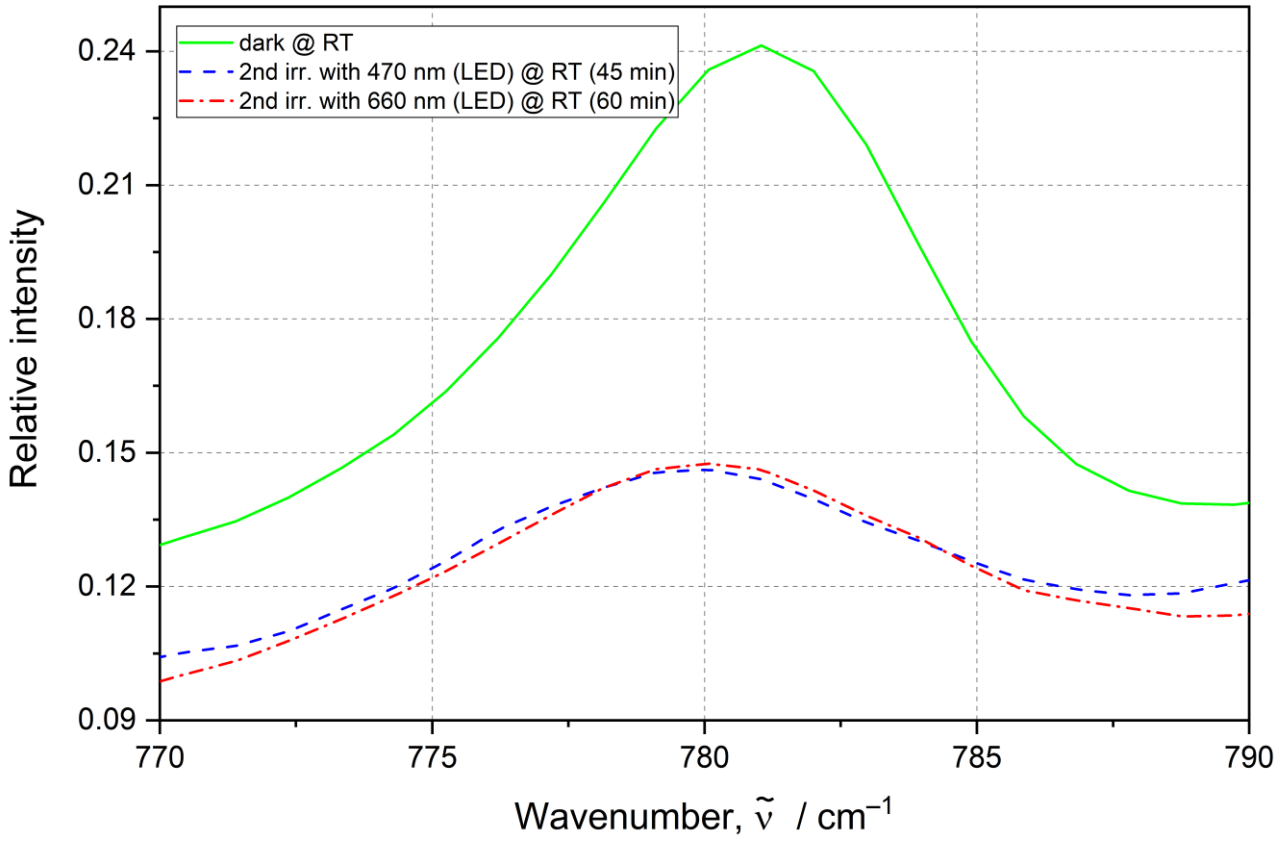

Figure 14S (continued). IR absorption spectra collected for [Co(Me-dpt)$(NO_2)_3$] in the solid state for the initial sample, after the 4th cycle of 470 and 660 nm LED light irradiation.

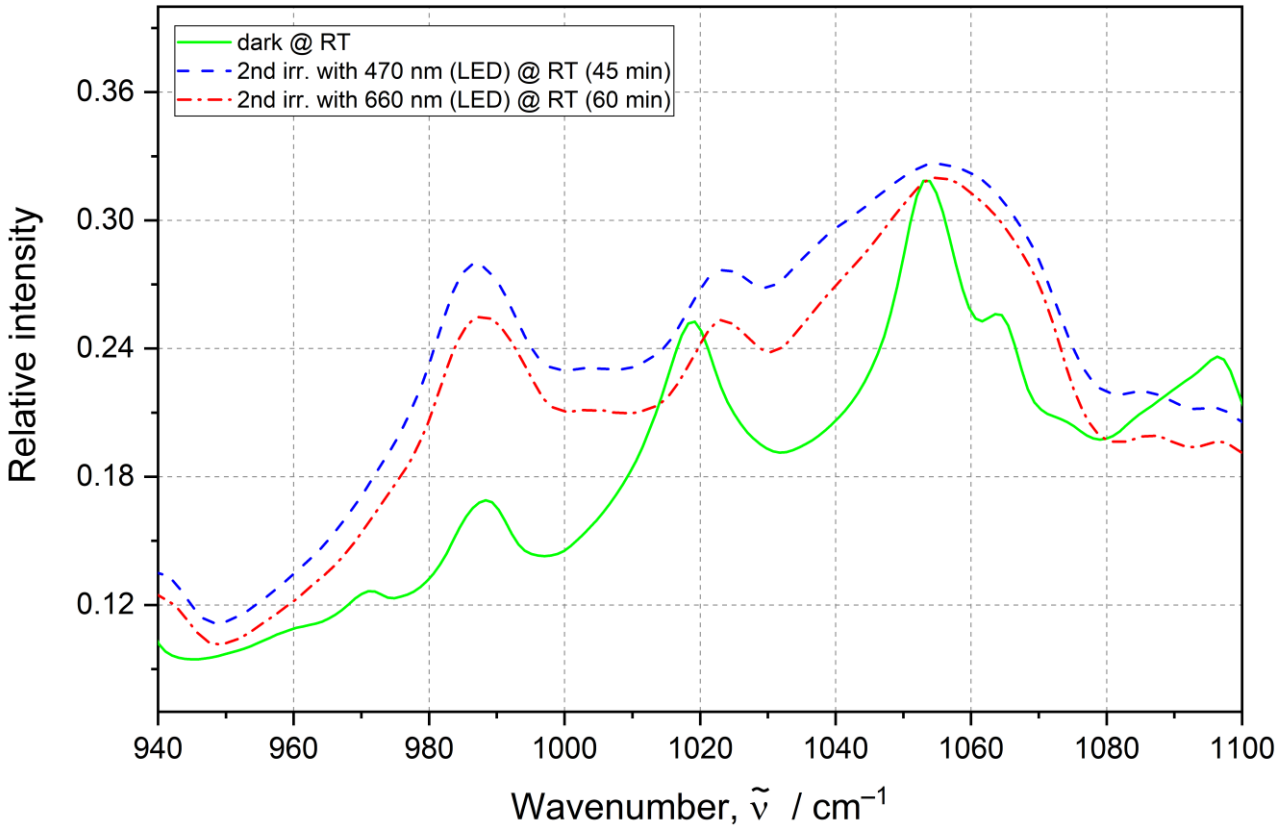

Figure 14S (continued). IR absorption spectra collected for [Co(Me-dpt)$(NO_2)_3$] in the solid state for the initial sample, after the 4th cycle of 470 and 660 nm LED light irradiation.

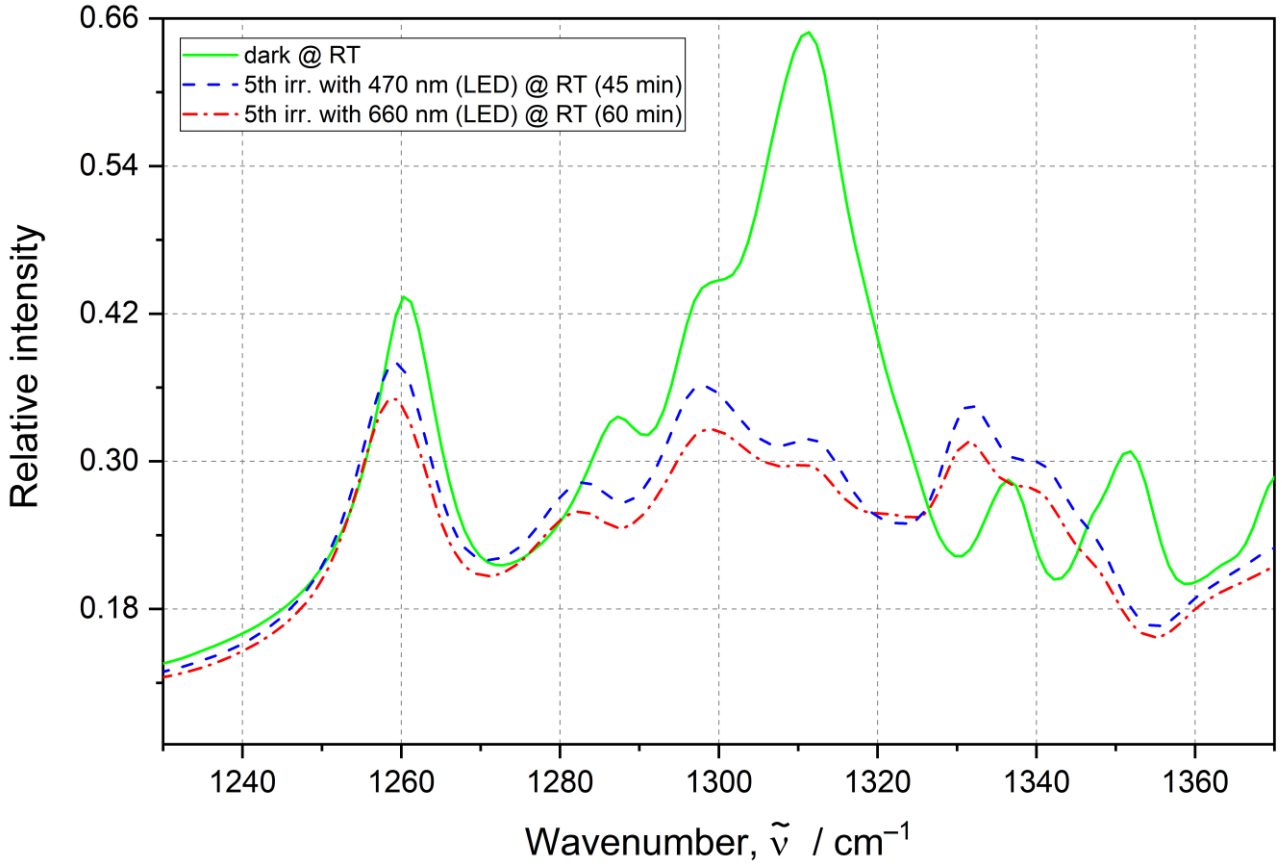

Figure 14S (continued). IR absorption spectra collected for [Co(Me-dpt)$(NO_2)_3$] in the solid state for the initial sample, after the 4th cycle of 470 and 660 nm LED light irradiation.

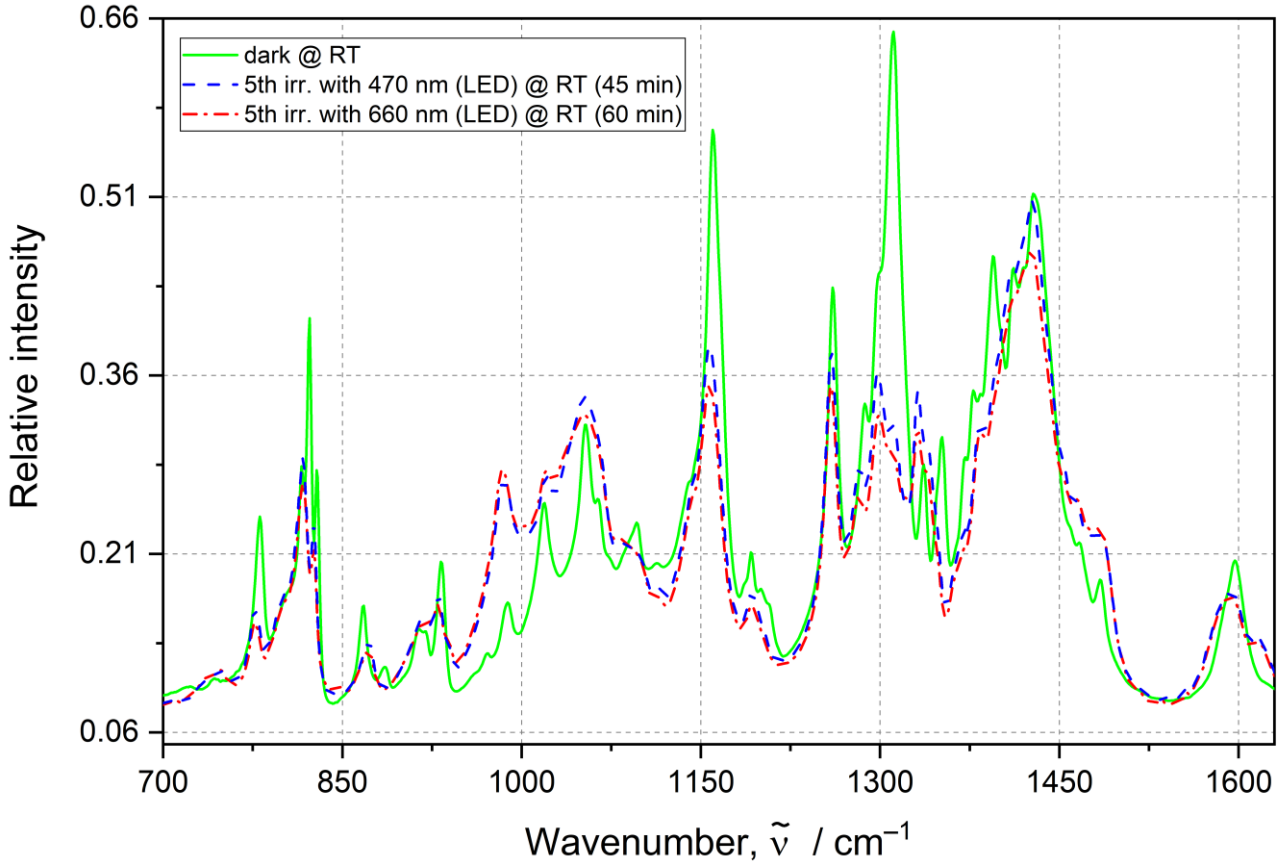

Figure 15S. IR absorption spectra collected for [Co(Me-dpt)$(NO_2)_3$] in the solid state for the initial sample, after the 5th cycle of 470 and 660 nm LED light irradiation.

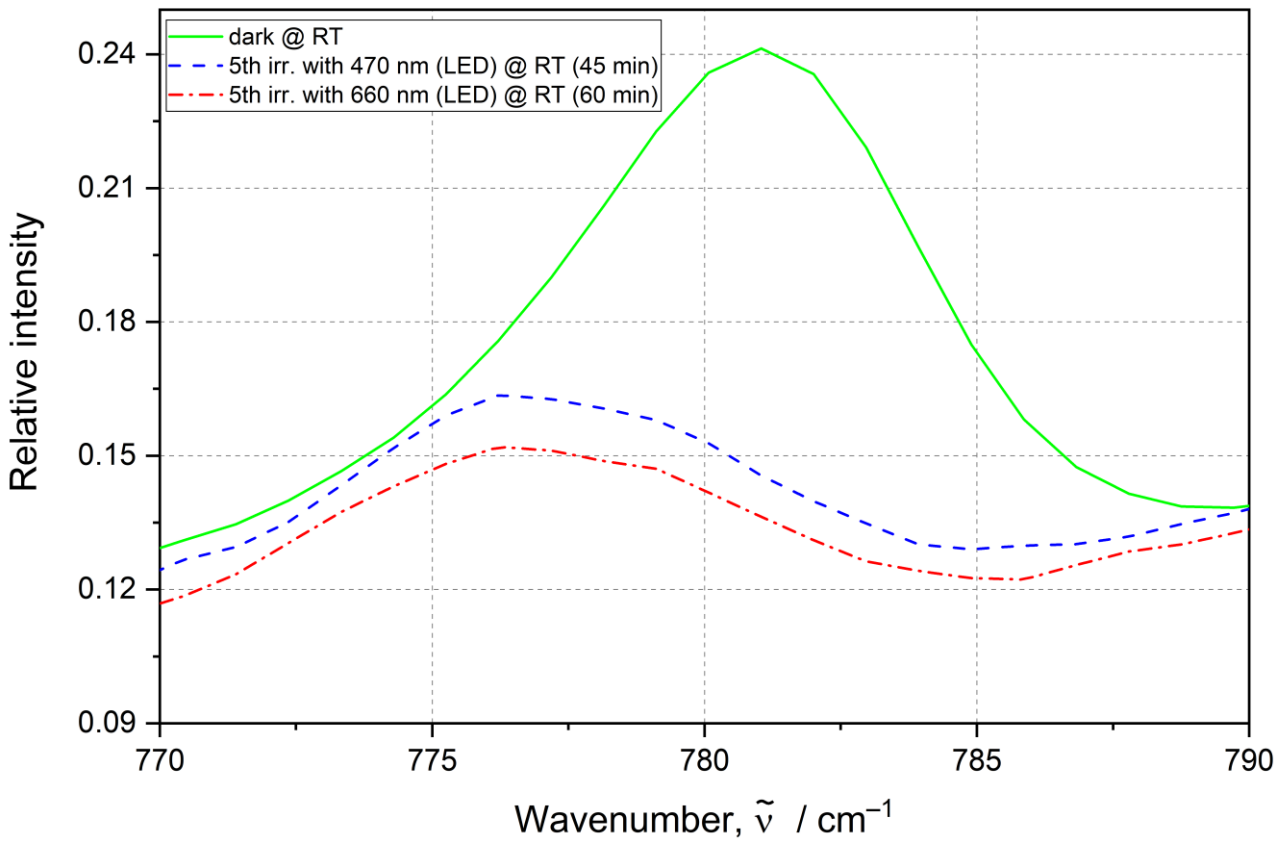

Figure 15S (continued). IR absorption spectra collected for [Co(Me-dpt)$(NO_2)_3$] in the solid state for the initial sample, after the 5th cycle of 470 and 660 nm LED light irradiation.

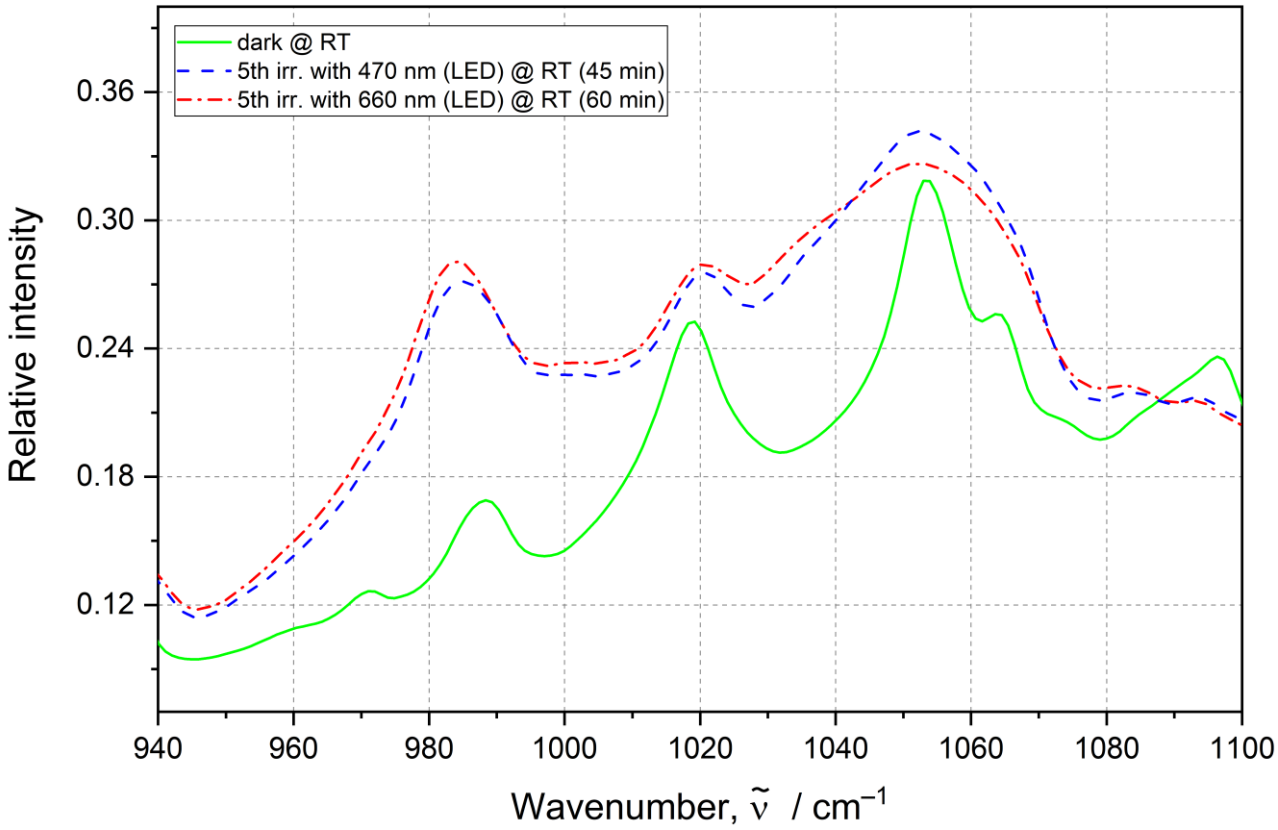

Figure 15S (continued). IR absorption spectra collected for [Co(Me-dpt)$(NO_2)_3$] in the solid state for the initial sample, after the 5th cycle of 470 and 660 nm LED light irradiation.

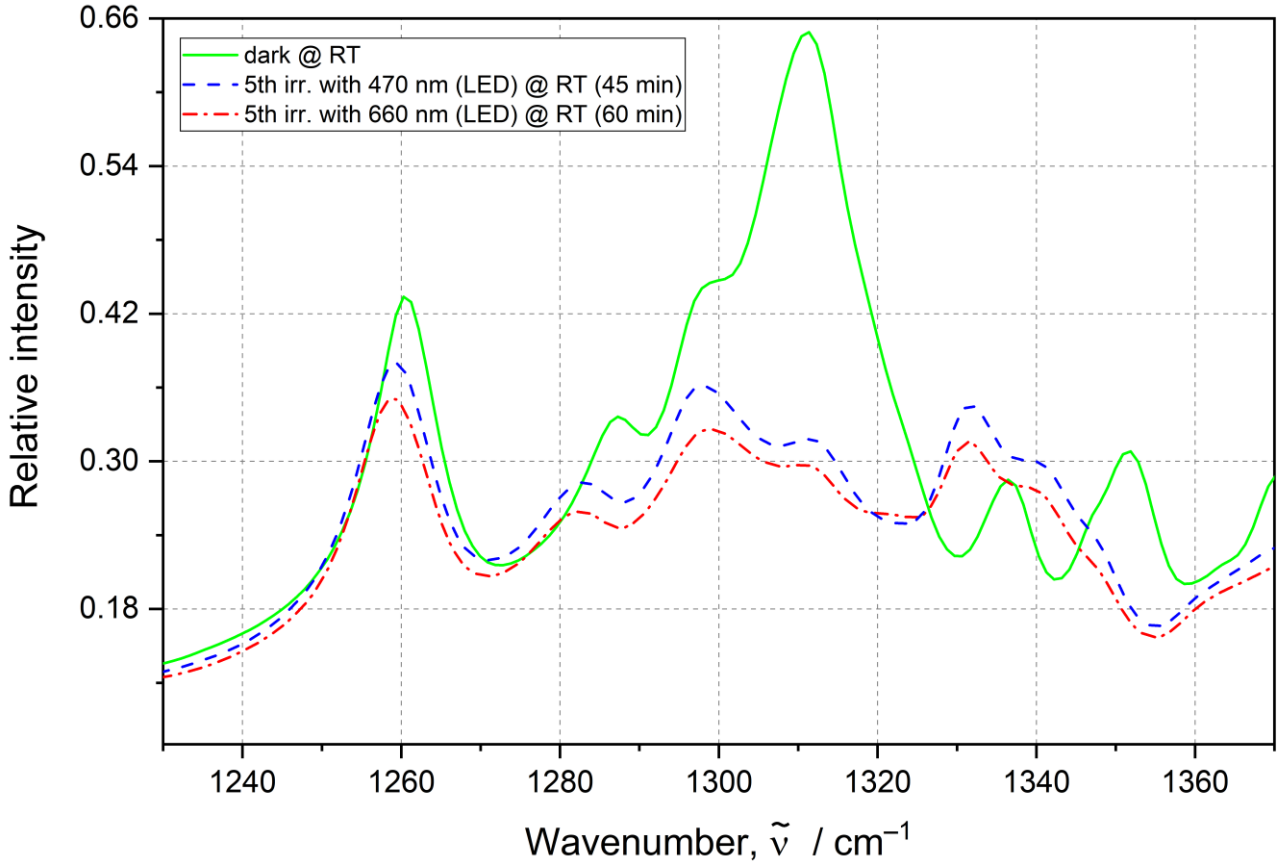

Figure 15S (continued). IR absorption spectra collected for [Co(Me-dpt)$(NO_2)_3$] in the solid state for the initial sample, after the 5th cycle of 470 and 660 nm LED light irradiation.

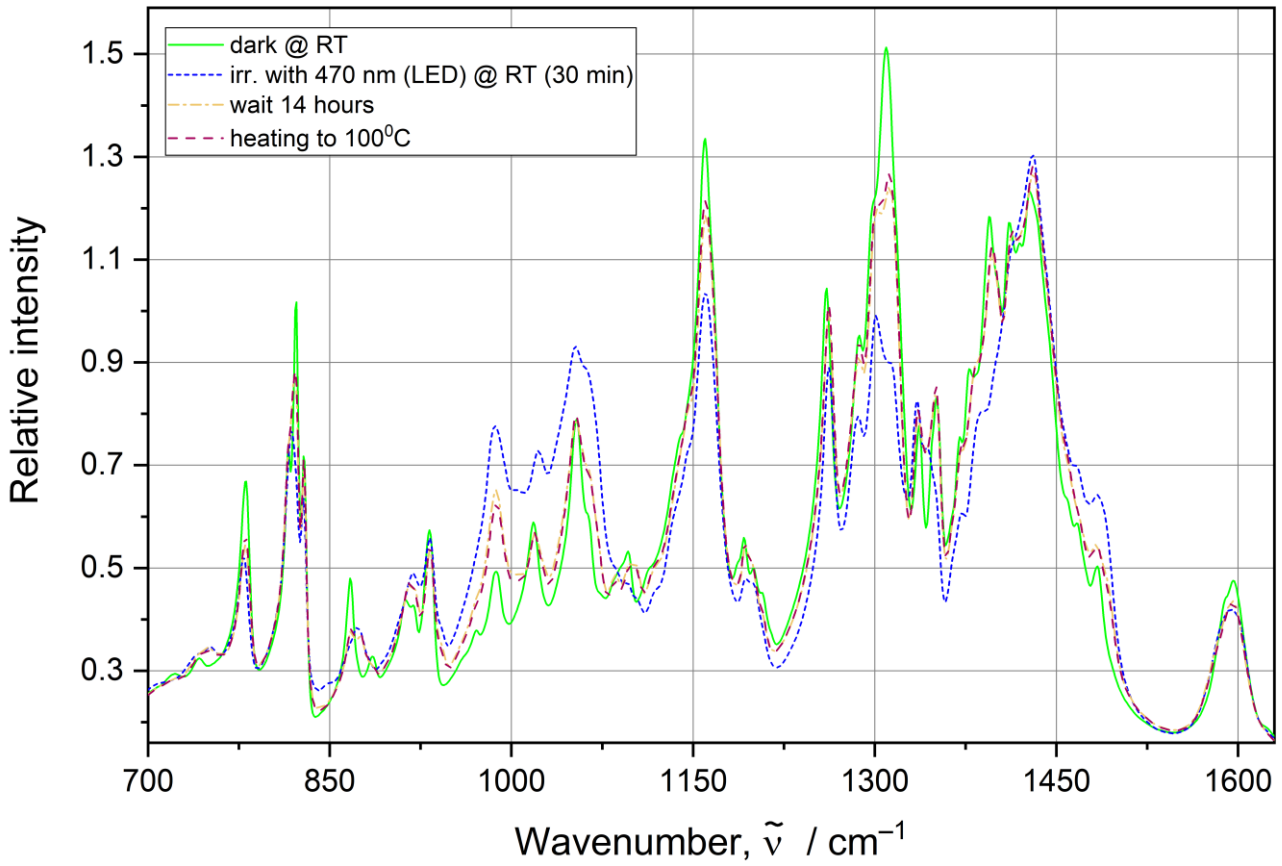

Figure 16S. IR solid-state absorption spectra collected for the same sample of [Co(Me-dpt)$(NO_2)_3$] – for the initial sample, after 470 nm LED light irradiation, after subsequent waiting for 14 hours, and finally – after heating to 100°C for 1 hour.

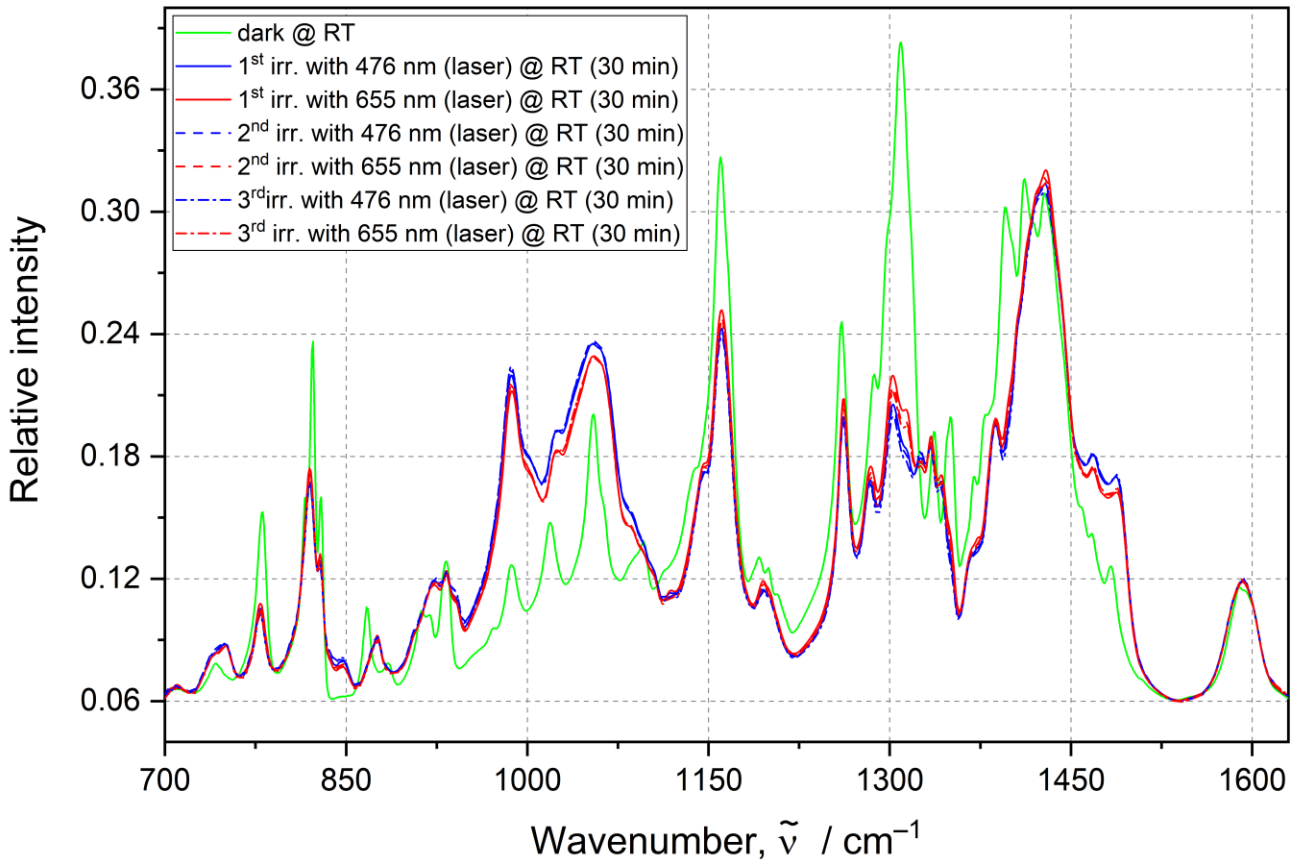

Figure 16S. IR absorption spectra collected for [Co(Me-dpt)$(NO_2)_3$] in the solid state showing changes after several cycles of 476 and 655 nm laser light irradiation.

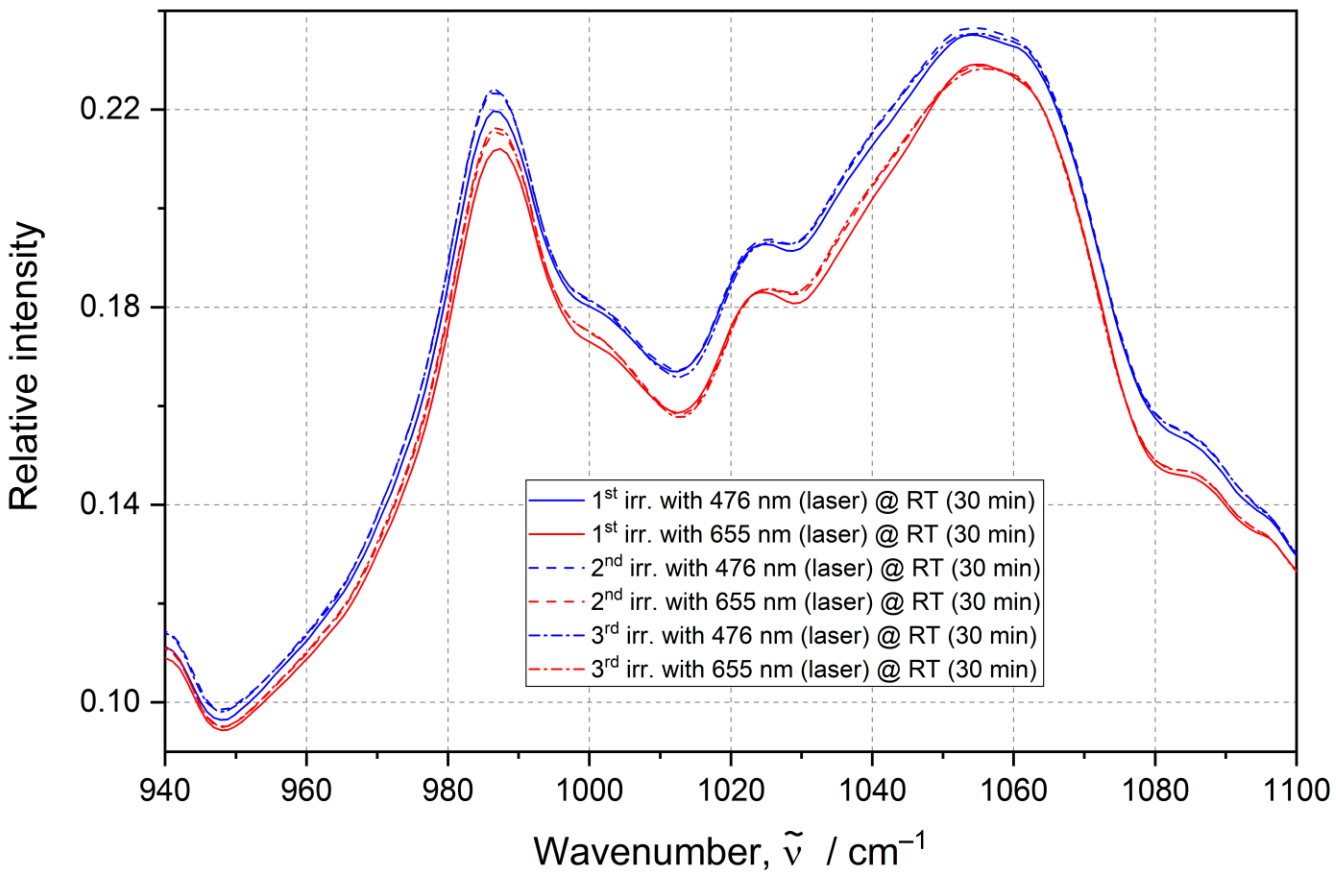

Figure 17S (continued). IR absorption spectra collected for [Co(Me-dpt)$(NO_2)_3$] in the solid state showing changes after several cycles of 476 and 655 nm laser light irradiation.

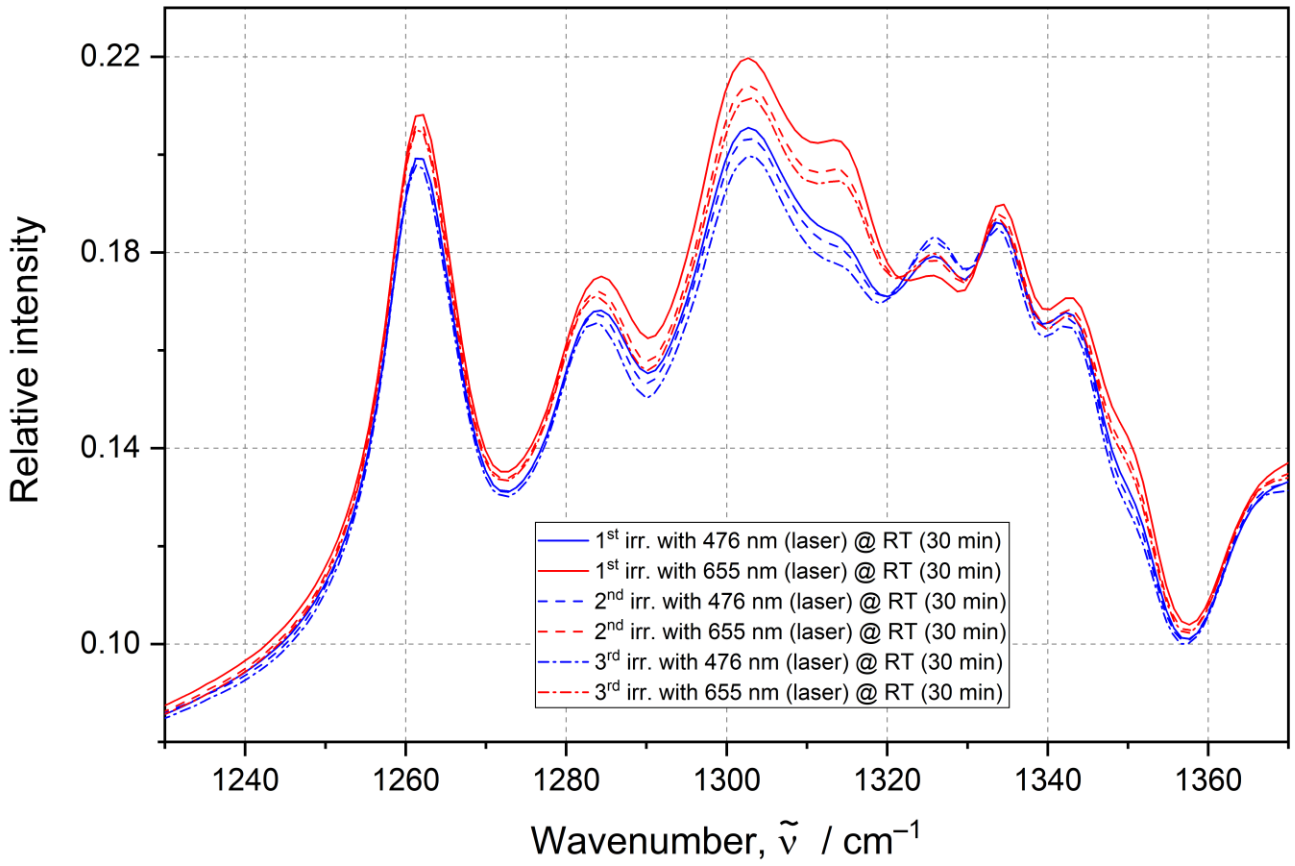

Figure 17S (continued). IR absorption spectra collected for [Co(Me-dpt)$(NO_2)_3$] in the solid state showing changes after several cycles of 476 and 655 nm laser light irradiation.

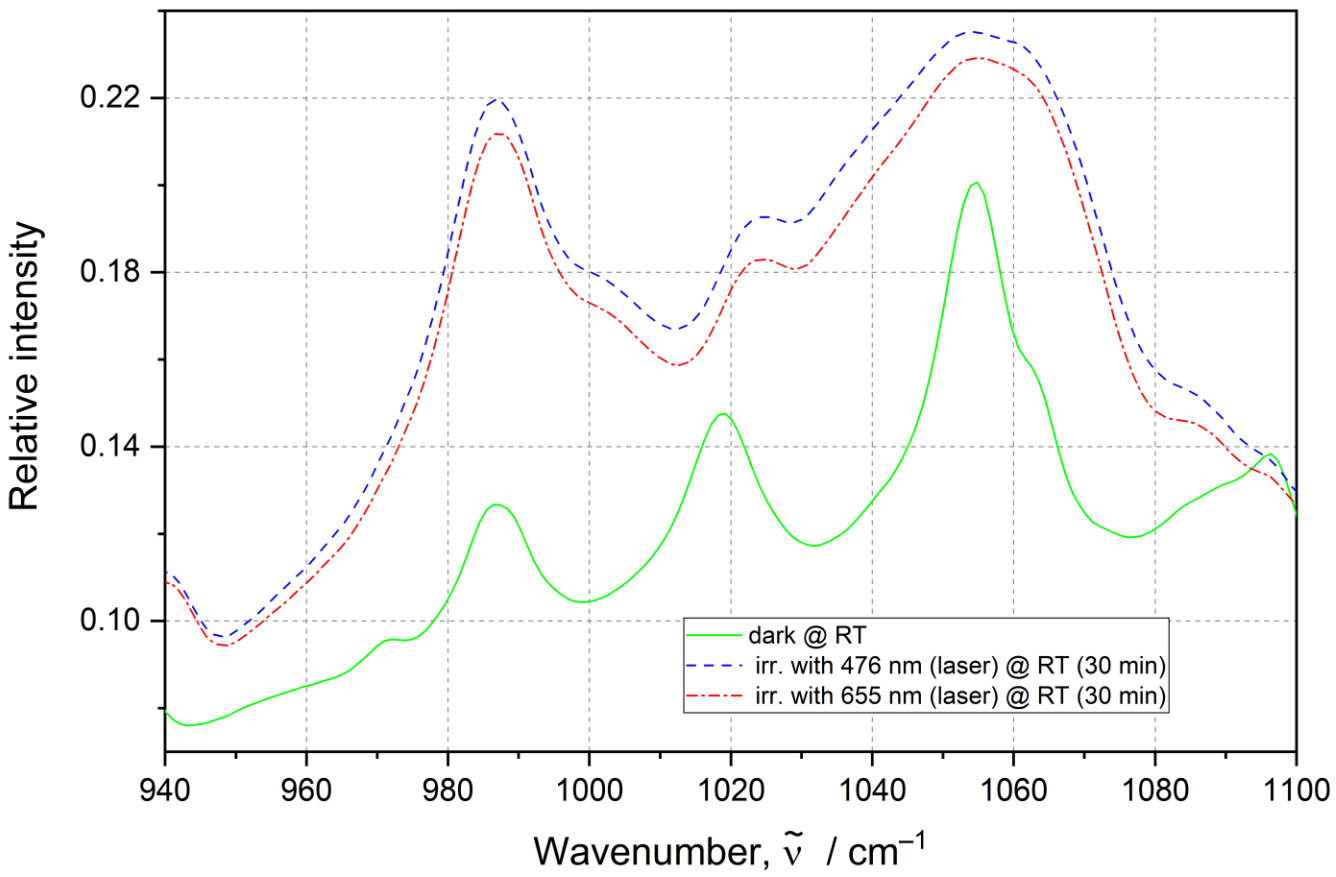

Figure 17S (continued). IR absorption spectra collected for [Co(Me-dpt)$(NO_2)_3$] in the solid state showing changes after the fisrt cycle of 476 and 655 nm laser light irradiation in respect to the dark RT reference.

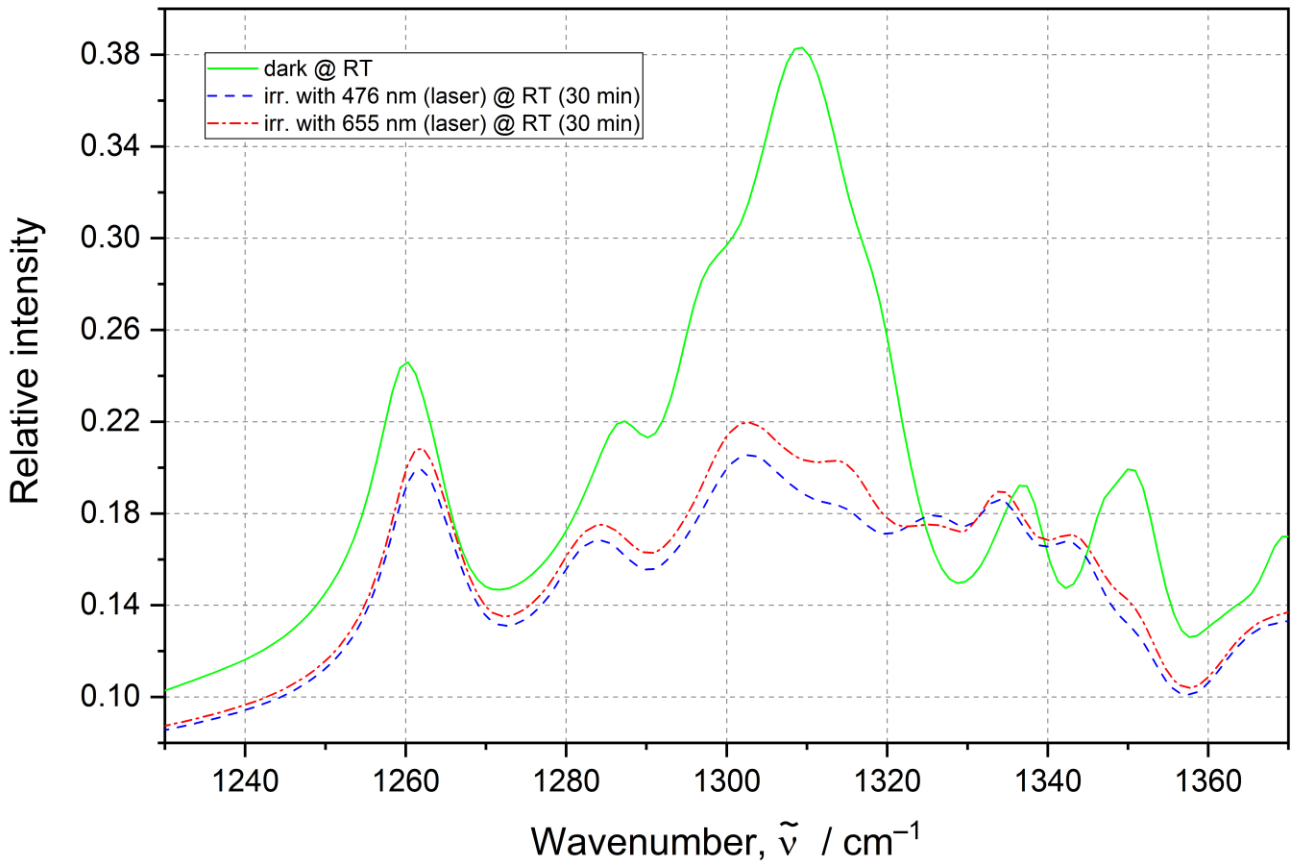

Figure 17S (continued). IR absorption spectra collected for [Co(Me-dpt)$(NO_2)_3$] in the solid state showing changes after the first cycle of 476 and 655 nm laser light irradiation in respect to the dark RT reference.

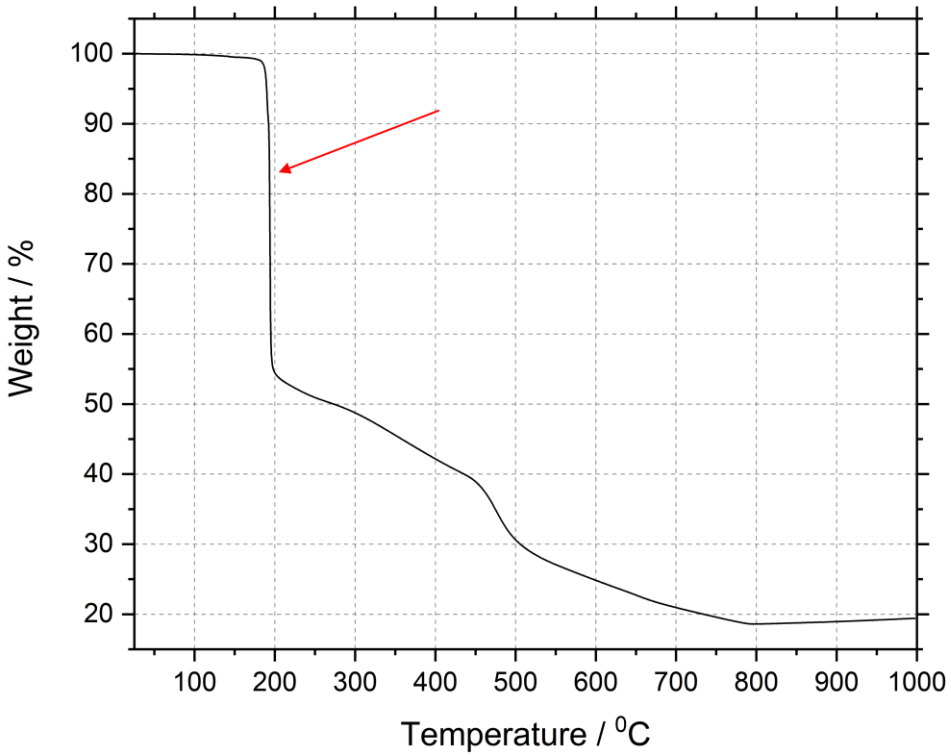

Figure 18S. TGA curve obtained for the [Co(Me-dpt)$(NO_2)_3$] complex when scanning within the 25–1000˚C temperature range. Red arrow shows area of crystal decomposition.

Table 12S. Theoretically calculated key vibrational modes (given in Hz) characteristic for the examined linkage isomers of the nitro group. $\delta(NO_2)$ – nitro NO_2 group scissoring mode, $\nu_{sym}(NO_2)$ – nitro NO_2 group symmetric stretching mode, $\nu_{asym}(NO_2)$ – nitro NO_2 group asymmetric stretching mode, $\nu(N{-}O)$ – nitrito N–O bond stretching mode, $\nu(N{=}O)$ – nitrito N=O bond stretching mode.

Mode	*Frequency*
$\delta(NO_2)$	836.58
	842.18
	850.75
$\nu_{sym}(NO_2)$	1359.06
	1370.01
	1402.66
$\nu_{asym}(NO_2)$	1480.73
	1534.89
$\nu(N{-}O)$	1060.87
$\nu(N{=}O)$	1545.09

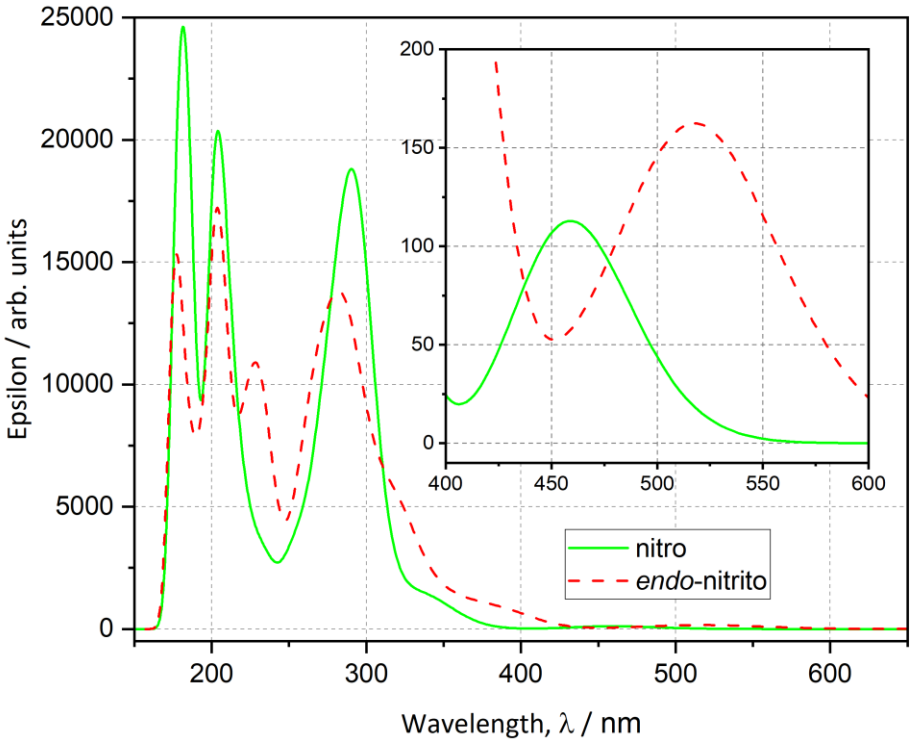

Figure 19S. Theoretical UV-Vis spectra computed at the DFT(B3LYP)/6-311++G** level of theory for the nitro (green solid line) and *endo*-nitrito (red dashed line) linkage isomers (QM/MM optimised geometries were used in the calculations).

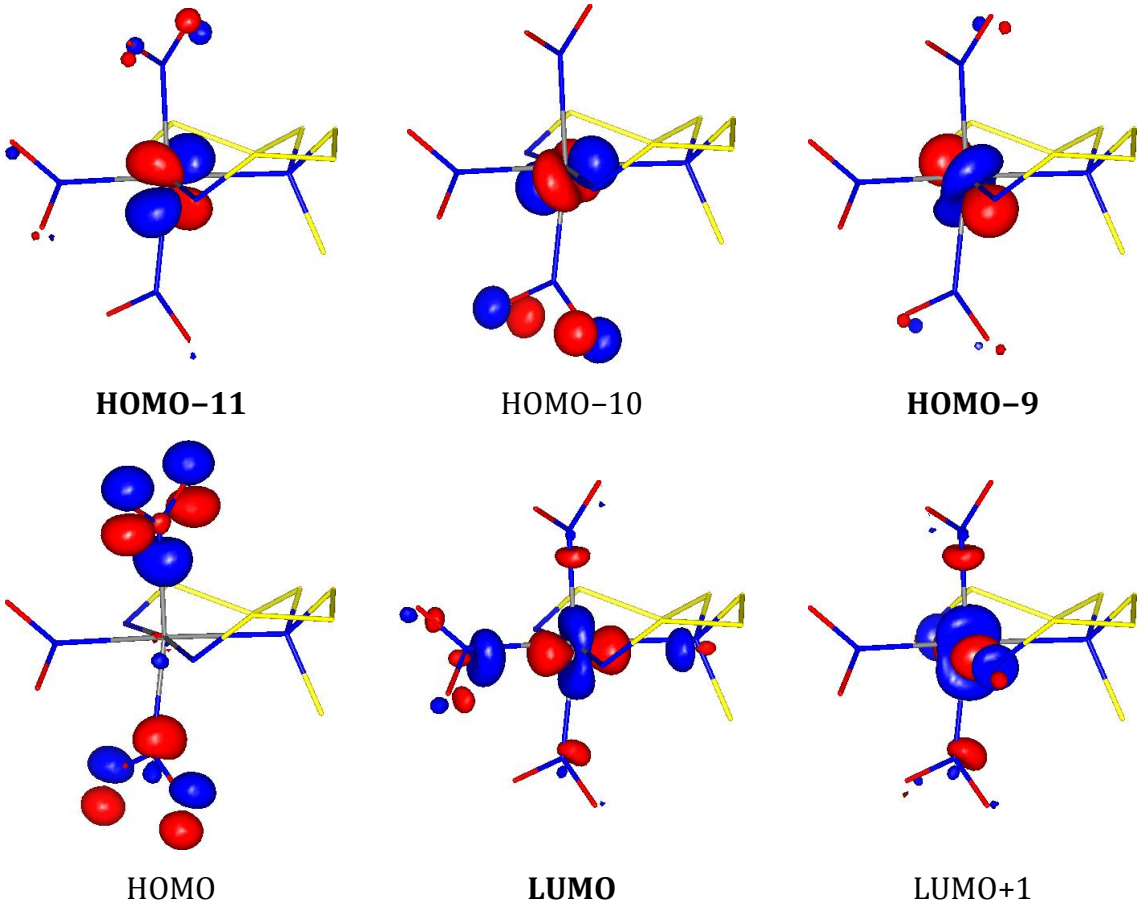

Figure 20S. Selected molecular orbitals (MOs) generated for the QM/MM-optimised nitro isomer of cobalt complex (DFT(B3LYP)/6-311++G** level of theory; ±0.1 a.u. blue surfaces – positive values, red – negative) with notable contributions to the lowest energy singlet-singlet electronic transitions (MOs with major contribution are written in bold).

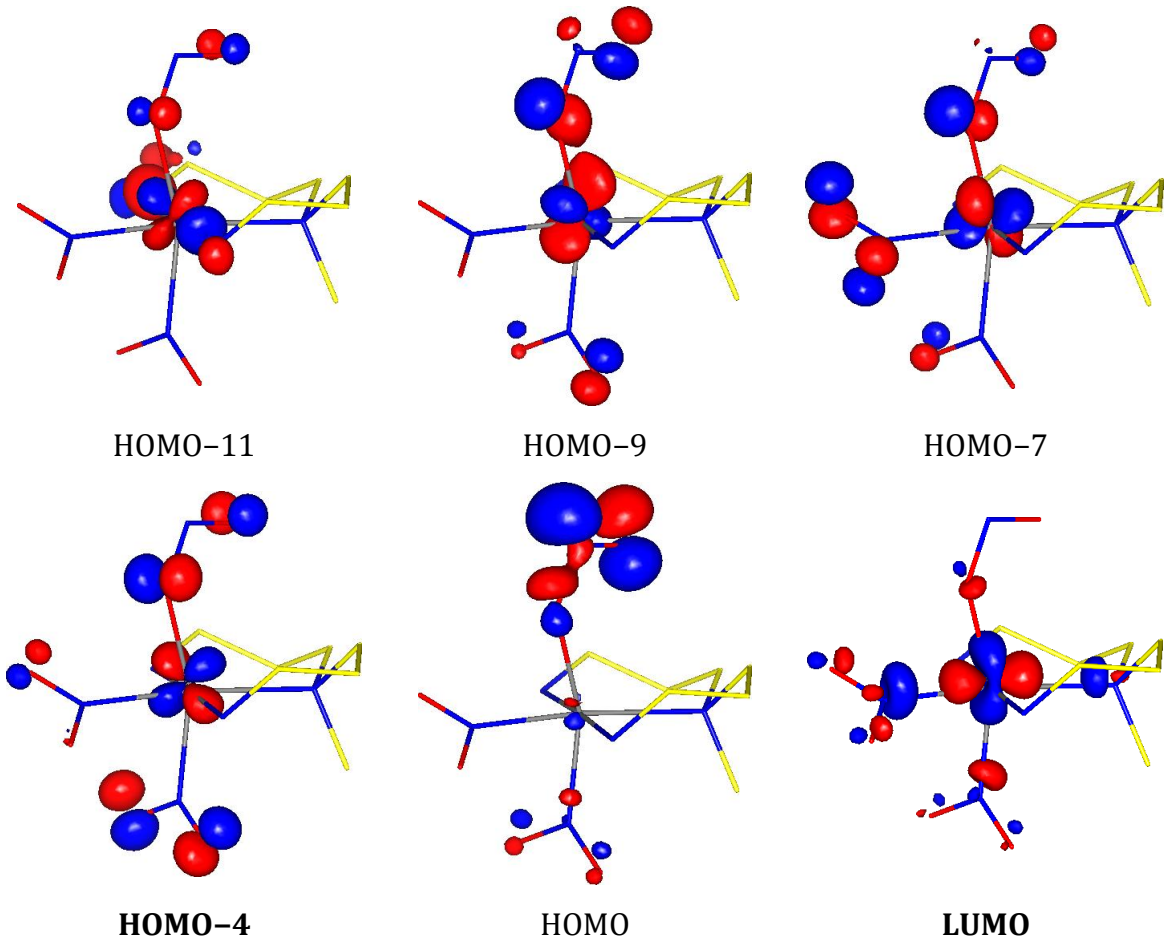

Figure 21S. Selected molecular orbitals generated for the QM/MM-optimised *endo*-nitrito isomer of cobalt complex (DFT(B3LYP)/6-311++G** level of theory; ±0.1 a.u. blue surfaces – positive values, red – negative) with notable contributions to the lowest energy singlet-singlet electronic transitions (MOs with major contribution are written in bold).

Extra references

1. U. Mukhopadhyay, I. Bernal, D. S. Yufit, J. A. K. Howard, L. Massa, A. Gindulyte, L. Todaro and S. S. Massoud, *Inorg. Chim. Acta*, 2004, **357**, 4121-4128.
2. R. Kamiński, K. N. Jarzembska, S. E. Kutyła and M. Kamiński, *J. Appl. Cryst.*, 2016, **49**, 1383-1387.
3. G. M. Sheldrick, *Acta Cryst. Sect. A*, 2015, **71**, 3-8.
4. V. Petříček, M. Dušek and L. Palatinus, *Z. Kristallogr.*, 2014, **229**, 345-352.
5. B. Fournier and P. Coppens, *Acta Cryst. Sect. A*, 2014, **70**, 291-299.
6. M. S. Schmøkel, R. Kamiński, J. B. Benedict and P. Coppens, *Acta Cryst. Sect. A*, 2010, **66**, 632-636.
7. F. H. Allen, *Acta Cryst. Sect. B*, 2002, **58**, 380-388.
8. C. R. Groom, I. J. Bruno, M. P. Lightfoot and S. C. Ward, *Acta Cryst. Sect. B*, 2016, **72**, 171-179.
9. A. Le Bail, H. Duroy and J. L. Fourquet, *Mater. Res. Bull.*, 1988, **23**, 447-452.
10. M. Dusek, V. Petricek, M. Wunschel, R. E. Dinnebier and S. van Smaalen, *J. Appl. Cryst.*, 2001, **34**, 398-404.
11. M. J. Frisch, G. W. Trucks, H. B. Schlegel, G. E. Scuseria, M. A. Robb, J. R. Cheeseman, G. Scalmani, V. Barone, G. A. Petersson, H. Nakatsuji, X. Li, M. Caricato, A. V. Marenich, J. Bloino, B. G. Janesko, R. Gomperts, B. Mennucci, H. P. Hratchian, J. V. Ortiz, A. F. Izmaylov, J. L. Sonnenberg, Williams, F. Ding, F. Lipparini, F. Egidi, J. Goings, B. Peng, A. Petrone, T. Henderson, D. Ranasinghe, V. G. Zakrzewski, J. Gao, N. Rega, G. Zheng, W. Liang, M. Hada, M. Ehara, K. Toyota, R. Fukuda, J. Hasegawa, M. Ishida, T. Nakajima, Y. Honda, O. Kitao, H. Nakai, T. Vreven, K. Throssell, J. A. Montgomery Jr., J. E. Peralta, F. Ogliaro, M. J. Bearpark, J. J. Heyd, E. N. Brothers, K. N. Kudin, V. N. Staroverov, T. A. Keith, R. Kobayashi, J. Normand, K. Raghavachari, A. P. Rendell, J. C. Burant, S. S. Iyengar, J. Tomasi, M. Cossi, J. M. Millam, M. Klene, C. Adamo, R. Cammi, J. W. Ochterski, R. L. Martin, K. Morokuma, O. Farkas, J. B. Foresman and D. J. Fox, *Journal*, 2016.
12. R. Kamiński, M. S. Schmøkel and P. Coppens, *J. Phys. Chem. Lett.*, 2010, **1**, 2349-2353.
13. F. H. Allen, O. Kennard, D. G. Watson, L. Brammer, A. G. Orpen and R. Taylor, *J. Chem. Soc., Perkin Trans. 2*, 1987, DOI: 10.1039/P298700000S1, S1-S19.
14. F. H. Allen and I. J. Bruno, *Acta Cryst. Sect. B*, 2010, **66**, 380-386.
15. A. D. Becke, *Phys. Rev. A*, 1988, **38**, 3098-3100.
16. J. P. Perdew, *Phys. Rev. B*, 1986, **33**, 8822-8824.
17. C. Lee, W. Yang and R. G. Parr, *Phys. Rev. B*, 1988, **37**, 785-789.
18. R. Krishnan, J. S. Binkley, R. Seeger and J. A. Pople, *J. Chem. Phys.*, 1980, **72**, 650-654.
19. T. Clark, J. Chandrasekhar, G. W. Spitznagel and P. v. R. Schleyer, *J. Comput. Chem.*, 1983, **4**, 294-301.
20. A. D. McLean and G. S. Chandler, *J. Chem. Phys.*, 1980, **72**, 5639-5648.
21. A. K. Rappé, C. J. Casewit, K. S. Colwell, W. A. G. III and W. M. Skiff, *J. Am. Chem. Soc.*, 1992, **114**, 10024-10035.
22. F. L. Hirshfeld, *Theor. Chim. Acta*, 1977, **44**, 129.

23. S. Grimme, *J. Comput. Chem.*, 2004, **25**, 1463-1473.
24. S. Grimme, *J. Comput. Chem.*, 2006, **27**, 1787-1799.
25. S. Grimme, J. Antony, S. Ehrlich and H. Krieg, *J. Chem. Phys.*, 2010, **132**, 154104.
26. S. Grimme, S. Ehrlich and L. Goerigk, *J. Comput. Chem.*, 2011, **32**, 1456-1465.
27. S. F. Boys and F. Bernardi, *Mol. Phys.*, 1970, **19**, 553-566.
28. S. Simon, M. Duran and J. J. Dannenberg, *J. Chem. Phys.*, 1996, **105**, 11024-11031.
29. R. Kamiński, K. N. Jarzembska and S. Domagała, *J. Appl. Cryst.*, 2013, **46**, 540-534.
30. M. R. Warren, S. K. Brayshaw, A. L. Johnson, S. Schiffers, P. R. Raithby, T. L. Easun, M. W. George, J. E. Warren and S. J. Teat, *Angewandte Chemie International Edition*, 2009, **48**, 5711-5714.
31. L. E. Hatcher, M. R. Warren, D. R. Allan, S. K. Brayshaw, A. L. Johnson, S. Fuertes, S. Schiffers, A. J. Stevenson, S. J. Teat, C. H. Woodall and P. R. Raithby, *Angewandte Chemie International Edition*, 2011, **50**, 8371-8374.
32. L. E. Hatcher, E. J. Bigos, M. J. Bryant, E. M. MacCready, T. P. Robinson, L. K. Saunders, L. H. Thomas, C. M. Beavers, S. J. Teat, J. Christensen and P. R. Raithby, *CrystEngComm*, 2014, **16**, 8263-8271.
33. S. E. Kutniewska, R. Kamiński, W. Buchowicz and K. N. Jarzembska, *Inorganic Chemistry*, 2019, **58**, 16712-16721.
34. S. E. Kutniewska, A. Krowczynski, R. Kaminski, K. N. Jarzembska, S. Pillet, E. Wenger and D. Schaniel, *IUCrJ*, 2020, **7**, 1188-1198.
35. L. E. Hatcher, *CrystEngComm*, 2016, **18**, 4180-4187.
36. I. Nakamura, R. Sumitani and T. Mochida, *Crystal Growth & Design*, 2021, **21**, 1861-1868.
37. M. R. Warren, T. L. Easun, S. K. Brayshaw, R. J. Deeth, M. W. George, A. L. Johnson, S. Schiffers, S. J. Teat, A. J. Warren, J. E. Warren, C. C. Wilson, C. H. Woodall and P. R. Raithby, *Chem. Eur. J.*, 2014, **20**, 5468-5477.
38. P. Borowski, S. E. Kutniewska, R. Kamiński, A. Krówczyński, D. Schaniel and K. N. Jarzembska, *Inorg. Chem.*, 2022, **61**, 6624-6640.
39. C. F. Macrae, I. J. Bruno, J. A. Chisholm, P. R. Edgington, P. McCabe, E. Pidcock, L. Rodriguez-Monge, R. Taylor, J. v. d. Streek and P. A. Wood, *J. Appl. Cryst.*, 2008, **41**, 466-470.